

Technical Report  
819

# New Techniques for High-Resolution Optical Space Surveillance

T.P. Wallace

2 November 1988

---

**Lincoln Laboratory**

MASSACHUSETTS INSTITUTE OF TECHNOLOGY

*LEXINGTON, MASSACHUSETTS*



---

Prepared for the Department of the Air Force  
under Electronic Systems Division Contract F19628-85-C-0002.

Approved for public release; distribution unlimited.

BEST AVAILABLE COPY

ADA202785

The work reported in this document was performed at Lincoln Laboratory, a center for research operated by Massachusetts Institute of Technology, with the support of the Department of the Air Force under Contract F19628-85-C-0002.

This report may be reproduced to satisfy needs of U.S. Government agencies.

The views and conclusions contained in this document are those of the contractor and should not be interpreted as necessarily representing the official policies, either expressed or implied, of the United States Government.

The ESD Public Affairs Office has reviewed this report, and it is releasable to the National Technical Information Service, where it will be available to the general public, including foreign nationals.

This technical report has been reviewed and is approved for publication.

FOR THE COMMANDER

*Hugh L. Southall*

Hugh L. Southall, Lt. Col., USAF  
Chief, ESD Lincoln Laboratory Project Office

Non-Lincoln Recipients

**PLEASE DO NOT RETURN**

Permission is given to destroy this document  
when it is no longer needed.

MASSACHUSETTS INSTITUTE OF TECHNOLOGY  
LINCOLN LABORATORY

**NEW TECHNIQUES FOR HIGH-RESOLUTION  
OPTICAL SPACE SURVEILLANCE**

*T.P. WALLACE*  
*Group 93*

TECHNICAL REPORT 819

2 NOVEMBER 1988

Approved for public release; distribution unlimited.

LEXINGTON

MASSACHUSETTS

## **ABSTRACT**

The problem of imaging through atmospheric turbulence has plagued astronomers for centuries. Only in the last 20 years has the lost resolution been restored through innovative hardware and algorithms. This report discusses the new optical imaging technologies of adaptive optics and speckle imaging in the space surveillance context. The techniques are compared and contrasted, and new imaging methods are proposed which combine elements of both. New methods are suggested for optical data evaluation.



## TABLE OF CONTENTS

<b>ABSTRACT</b>	iii
<b>LIST OF ILLUSTRATIONS</b>	vii
<b>1. INTRODUCTION</b>	1
<b>2. OVERVIEW</b>	3
2.1 Optics	3
2.2 Physical Model	3
2.3 Adaptive Optics	3
2.4 Speckle Imaging	4
<b>3. STATISTICAL OPTICS</b>	5
3.1 Introduction	5
3.2 Propagation of Light	5
3.3 Optical Coherence	7
3.4 The Van Cittert-Zernike Theorem	12
3.5 Propagation Through Transmitting Objects	13
3.6 The Interferometric View of Imaging	15
<b>4. ATMOSPHERIC TURBULENCE</b>	17
4.1 Introduction	17
4.2 Statistical Representation of Atmospheric Parameters	17
4.3 Physics of Turbulence	18
4.4 Optical Propagation Through Turbulence	18
4.5 Summary	20
<b>5. ADAPTIVE OPTICS</b>	23
5.1 Overview	23
5.2 History	24
5.3 MPM Description	25
5.4 Wavefront Sensor Description	26
5.5 Processor	28
<b>6. SPECKLE IMAGING</b>	31
6.1 Speckle Interferometry	31

6.2 Phase Retrieval for Speckle Imaging	35
6.3 Speckle Parameters	40
<b>7. APPLICATION TO SPACE SURVEILLANCE</b>	<b>47</b>
7.1 Introduction	47
7.2 Generalized Optical Surveillance	47
7.3 Special Problems of Satellite Imaging	53
7.4 Analysis of Small Amplitude and Phase Errors	57
7.5 Selecting a Phase-Retrieval Algorithm	59
7.6 Optical Data Resolution Evaluation	60
<b>8. SUMMARY AND CONCLUSIONS</b>	<b>69</b>
<b>APPENDIX A – ANALYTIC SIGNALS</b>	<b>71</b>
<b>APPENDIX B – STRUCTURE FUNCTIONS</b>	<b>73</b>
<b>REFERENCES</b>	<b>75</b>

## LIST OF ILLUSTRATIONS

Figure No.	Page
3.1 Propagation Geometry	6
3.2 Typical Fringe Pattern with Envelope	8
3.3 Young's Interference Experiment	9
3.4 Mutual Coherence Propagation Geometry	11
3.5 Interferometric Imaging Model	16
5.1 Adaptive Optics Systems	24
5.2 Variable-Shear Rotary AC Interferometer	27
5.3 Wavefront Reconstruction	29
6.1 Schematic Speckle Imaging	32
6.2 Turbulence MTF for Labeyrie (solid), Long-Term Exposure (dotted)	34
6.3 Gerchberg-Saxton Algorithm	39
6.4 Fienup's Algorithm	39
7.1 Generalized Optical Surveillance System	48
7.2 Circular Aperture Transfer Function	50
7.3 Effects of Coherent Integration	51
7.4 Satellite Imaging Geometry	54
7.5 Imaging a Solar Panel	55
7.6 Maximum Integration Time for Specified Resolution	56
7.7 Simulated MTF of Random Phase Errors	58
7.8 Typical Image Evaluation Functions	62
7.9 Joint Probability Density Functions of $\phi_1(f)$ , $\phi_2(f)$	63
7.10 Evaluation Functions for Simulated Data	65
7.11 Sample Correlation Function for the Data of Fig. 7.10	67

# 1. INTRODUCTION

Optical study of space objects has faced atmospheric limitations to resolution for centuries. One finds that increasing a lens diameter beyond about 10 cm is ineffective in increasing telescope resolution. Light-gathering ability increases, but atmospheric turbulence prevents a corresponding increase in resolution.

In the last 15 years, two new and exciting approaches to imaging through turbulence, *adaptive optics* and *speckle imaging* have proven able to greatly reduce the degrading effects of turbulence in some cases. This offers hope that ground-based optical sensors may become contributors to the high-resolution imaging of space objects, an area now dominated by radar. There may also be opportunities for data fusion, combining information from optical and radar sensors.

One current sensor of interest is the AMOS/MOTIF (ARPA Maui Optical Station/Maui Optical Tracking and Identification Facility) Compensated Imaging System (CIS). This adaptive optics device has been able to provide high-resolution satellite images in some cases.

The adaptive optics approach requires complicated mechanical equipment in a feedback control arrangement. There is extensive real-time processing required, but the algorithms are relatively straightforward. The speckle approach requires simpler hardware, but utilizes extensive non-real-time processing with innovative and complicated algorithms.

These two new technologies have a lot in common, but the literature is fairly disjoint. This report will attempt to explain the relationships between them, as well as discuss the special problems of satellite surveillance. There is some synergy between these areas which can benefit each of them.

One question addressed by this report is whether or not the algorithms recently developed for speckle processing may be used to post-process adaptive optics data, increasing the effective resolution. One obviously cannot combine these techniques in the other order, i. e., once data have been collected for speckle processing it is too late to apply adaptive optics. It is possible, however, that the adaptive optics approach may suggest new or improved speckle processing algorithms.

This report is written from the point of view of signal processing and systems engineering. The required background for this report includes random process theory, basic digital signal processing, and basic physics.

To gain a complete understanding of these techniques requires background in physics, optics, astronomy, control theory, signal processing, mathematical optimization, and computer science, among other subjects. Sections 2-6 of this report will present a fair amount of background material on optics, turbulence, adaptive optics, and speckle processing to make the analysis accessible to those not trained in optics. The goal is to provide sufficient detail that the physics of the situation will become clear, quantitative calculations can be made, and the reader can consult the literature for details and new developments. Derivations of well-known results will be left to the references.

Section 7 will attempt to present a more unified analysis of the new optical technologies, and discuss satellite imaging problems in more detail. The new results are primarily confined to this section. These include an analysis of adaptive optics errors and a proposed method for speckle data evaluation. The reader who is well acquainted with speckle processing and adaptive optics is encouraged to start with Section 7, returning to previous sections only as necessary.



## 2. OVERVIEW

### 2.1 OPTICS

In radar and communications, we often deal with coherent, narrowband systems. We can envision waves propagating through space, and directly detect and process them coherently. While antennas are often two-dimensional, the signals are quickly beamformed into individual time functions.

In optics, we often deal with thermal light, e. g., light emitted from excited atoms in some random configuration. The resulting signal is a sample from a random process which is wideband and non-coherent. We also are generally interested in image formation, so rather than time functions we have functions of two or three spatial dimensions plus time.

The best way to handle such signals is to use what is known as the *analytic signal* representation. This method is occasionally used in the study of modulation and demodulation in communications, but is more prevalent in statistical optics. Our goal is to discuss the propagation of mutual coherence functions and the important Van Cittert-Zernike Theorem.

### 2.2 PHYSICAL MODEL

The physical situations of interest in this report may be described as follows. In the first case, an astronomical object emits thermal light. In the second case, radiation from a source of thermal light (such as the sun) is reflected from a satellite. In both cases, the light travels through the atmosphere and is modified by turbulent layers before entering the aperture of a telescope. The thermal light is best modeled as a random process, and the atmosphere likewise fluctuates randomly.

The limiting resolution which a telescope can provide is approximately

$$\theta = \frac{\lambda}{D} \quad (2.1)$$

where  $D$  is the telescope diameter and  $\lambda$  is the wavelength. The effects of turbulence can be included in this expression by replacing the telescope diameter  $D$  by an effective  $D$ . In areas of good astronomical “seeing” a long film exposure gives an effective  $D$  of about 10 cm. For example, with  $\lambda = 500$  nm, the resolvable angle  $\theta$  is  $5 \cdot 10^{-6}$  rad, or about 1” (second of arc). The light collected is proportional to the area of the telescope, but the resolution does not improve as  $D$  increases beyond 10 cm.

Another way of looking at this is in the frequency domain. If we take the two-dimensional Fourier transform of such an image, spatial frequencies greater than about one cycle/arc sec in either direction will be small.

### 2.3 ADAPTIVE OPTICS

Adaptive optics has been discussed and even implemented as long ago as the 1950s. The idea is not new, but the bandwidths of the original systems were in the region of several Hz instead of the several hundred or thousand Hz required to correct atmospheric turbulence. Hardy’s useful survey<sup>1</sup> discusses these early efforts. The first reported high-bandwidth adaptive optics system was produced<sup>2</sup> in 1973. The monolithic piezoelectric mirror (MPM) is the device which mechanically deforms at high

rates in response to the controlling voltage. Interferometers and an analog computer are the other key components in this system.

Atmospheric turbulence will be described in greater detail below, but during periods of good seeing, the major effect of turbulence is phase shifting due to path length variations; the amplitudes of the light are not greatly affected. In theory, mechanically deforming a mirror in the light path can perfectly correct the phase. Since the residual amplitude error is much less, we approach the diffraction limit in resolution.

## 2.4 SPECKLE IMAGING

In 1970 Labeyrie published a landmark paper<sup>3</sup> ushering in the era of speckle processing. Notationally, let  $f(x,y)$  be the image, and  $F(u,v)$  its Fourier transform. Labeyrie's insight was that although one could not achieve the diffraction limit by time averaging  $f(x,y)$  (long film exposure) things improved greatly when the quantity  $|F(u,v)|^2$  was time averaged.

If we average the spatial frequencies  $F(u,v)$ , we are averaging many complex quantities with zero mean so our result tends toward zero. (Note that averaging  $f(x,y)$  is equivalent to averaging  $F(u,v)$ , by linearity.) On the other hand, if we average the squared magnitudes of the spatial frequencies (the power spectrum) we are averaging positive quantities so the resultant does not tend toward zero.

From  $F(u,v)$ , one could retrieve the desired high-resolution image using an inverse Fourier transform. However, only  $|F(u,v)|^2$ , the power spectrum, is available. The inverse transform of  $|F(u,v)|^2$  is the autocorrelation function of the image, not the image itself. If we are only trying to measure binary star separations we may have all the information we need, but high-resolution imaging does not fall out immediately. We can take  $\sqrt{|F(u,v)|^2}$  and obtain the correct magnitude of  $F(u,v)$  but we are lacking the phases.

The phase retrieval problem will be discussed in more detail below, but suffice it to say that there exist practical methods for reconstructing the phase of  $F(u,v)$  in many cases. This is an area of current research, but major steps have been taken in the last ten years. Coupling Labeyrie's method for estimating  $|F(u,v)|$  with one or more of the phase reconstruction algorithms yields a complete high-resolution imaging capability.

### 3. STATISTICAL OPTICS

#### 3.1 INTRODUCTION

The optical theory required by this report is well presented in the book by Goodman.<sup>4</sup> We will extract some information from it in roughly the same order Goodman presents it. Goodman devotes two chapters to summarizing the theory of random processes. A more expanded treatment of this topic may be found in Papoulis<sup>5</sup> and similar texts. We will assume that the reader is familiar with this material.

An additional topic of interest is a short review of the theory of analytic signals. Appendix A will discuss this subject in as much detail as required here.

The first topic of the next subsection will be first-order properties of light, i. e., light properties at a single instant in time. We will discuss propagation of light waves of various bandwidths using the Huygens-Fresnel principle. We will define the instantaneous intensity (that quantity to which optical detectors respond).

At this point, we will consider second-order properties of light in the form of coherence functions. These include temporal and spatial coherence functions, the mutual coherence function, and mutual intensity. This material is needed to understand the operation of interferometers, the sensing elements of adaptive optics.

Propagation of mutual intensity from an incoherent source is described by the Van Cittert-Zemike theorem, the basis for speckle imaging. This theorem states that the mutual intensity is the two-dimensional Fourier transform of the intensity distribution across the source. This is reminiscent of the relationship of the illumination function of an antenna and the far field, but the quantities are entirely different.

Other material falling in the category of statistical optics relates directly to succeeding major sections of this report, and will be covered in those sections.

#### 3.2 PROPAGATION OF LIGHT

##### 3.2.1 Propagation of Monochromatic Light

Consider the scalar amplitude of one polarization component of the electrical or magnetic field of monochromatic light. If  $P$  represents a position in space and  $t$  a point in time, we will denote this amplitude  $u(P, t)$ . The analytic signal representation of  $u(P, t)$  is

$$u(P, t) = U(P, \nu) e^{-j2\pi\nu t} \quad (3.1)$$

where  $\nu$  is the frequency of the wave and  $U(P, \nu)$  is its amplitude. Let such a wave be incident from the left on the infinite surface  $\Sigma$  shown in Figure 3.1.

We are interested in the phasor amplitude of the field at the point  $P_0$  in terms of the field on  $\Sigma$ . We will use the approximation known as the Huygens-Fresnel principle. If  $c$  is the speed of light,  $\lambda = \frac{c}{\nu}$  is the wavelength,  $\chi(\theta)$  is an obliquity factor with  $\chi(0) = 1$  and  $0 \leq \chi(\theta) \leq 1$ , and  $r \gg \lambda$ ,



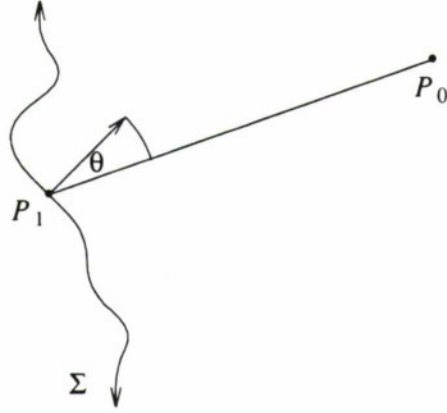


Figure 3.1. Propagation geometry.

$$U(P_0, \nu) = \frac{1}{j\lambda} \iint_{\Sigma} U(P_1, \nu) \frac{e^{j2\pi(r/\lambda)}}{r} \chi(\theta) dS. \quad (3.2)$$

Note from Figure 3.1 that  $\theta$  is the angle between the line connecting  $P_0$  and  $P_1$  and the normal to  $\Sigma$ . In words, each point on  $\Sigma$  acts as a secondary source of spherical waves radiating with directional amplitude pattern  $\chi(\theta)$ . More detail on the Huygens-Fresnel principle may be obtained from any text on optics.

### 3.2.2 Propagation of Nonmonochromatic Light

Since monochromatic light is of limited interest to us, we want to generalize our expression for light propagation. Let  $u(P, t)$  be a wave whose analytic representation is denoted  $\mathbf{u}(P, t)$ . It is possible to apply the Huygens-Fresnel principle inside of an integral over frequency to obtain an expression for general propagation. The main complication is that since  $u(P, t)$  may not be Fourier transformable, a truncated interval is used in the derivation and a limit is later taken. After a little manipulation, we obtain

$$\mathbf{u}(P_0, t) = \iint_{\Sigma} \frac{\frac{d}{dt} \mathbf{u}(P_1, t - r/c)}{2\pi cr} \chi(\theta) dS. \quad (3.3)$$

### 3.2.3 Propagation of Narrowband Light

If the light bandwidth  $\Delta\nu$  is much smaller than the center frequency  $\bar{\nu}$ , the propagation condition may be simplified to

$$\mathbf{u}(P_0, t) \approx \iint_{\Sigma} \frac{\mathbf{u}(P_1, t - r/c)}{j\lambda r} \chi(\theta) dS. \quad (3.4)$$



### 3.3 OPTICAL COHERENCE

#### 3.3.1 Temporal Coherence

If  $u(P, t)$  is the analytic signal corresponding to an optical wave, consider the relationship between  $u(P, t)$  and  $u(P, t + \tau)$ .  $u(P, t)$  has some bandwidth  $\Delta\nu$ , and hence the complex envelope  $|u(P, t)|$  is varying at a rate determined by  $\Delta\nu$ . If  $\tau \ll 1/\Delta\nu$  we expect  $u(P, t)$  and  $u(P, t + \tau)$  to be highly correlated.

At this point, we will digress with a word about detectors. Optical detectors respond to the intensity of the optical wave, e. g., the square of the magnitude of the analytic signal representation. We know the magnitude of the analytic signal as the complex envelope. The only thing to keep in mind is that most detectors average over a considerable amount of time. We are really recording some average of the square of the complex envelope.

The canonical experiment in temporal coherence was performed by Michelson in the 19th century. In the Michelson interferometer, a point source of light is split by a beam splitter and reflected from two different perpendicular mirrors, producing a selected path length difference. A detector records the resulting average intensity.

Mathematically, if we let the path difference be  $h$ , the time delay is  $\tau = h/c$ . The measured intensity will be

$$I(\tau) = \langle |u(t) + u(t + \tau)|^2 \rangle \quad (3.5)$$

where the angle brackets denote a time average. This will look something like Figure 3.2. For small path differences (time delays) everything is in phase and reinforces. As the delay increases, we see periodic behavior at the average wavelength  $\bar{\lambda}$ , but for larger delays, the multiple frequencies present in the wave cause dispersion and eventually result in a constant value with no fringes. There are fringes present at each individual frequency, but they add up in random phase to a constant value.

The exact behavior of a given optical wave depends on the bandwidth of that wave, or, more generally, on its spectral density. Much more can be said about this subject but we will not need it for our development.

If we expand Equation (3.5) and define the average intensity

$$I_0 \equiv \langle |u(t)|^2 \rangle \quad (3.6)$$

and the self-coherence function

$$\Gamma(\tau) \equiv \langle u(t + \tau) u^*(t) \rangle \quad (3.7)$$

we obtain

$$I(\tau) = 2\{I_0 + \text{Re} [\Gamma(\tau)]\}. \quad (3.8)$$

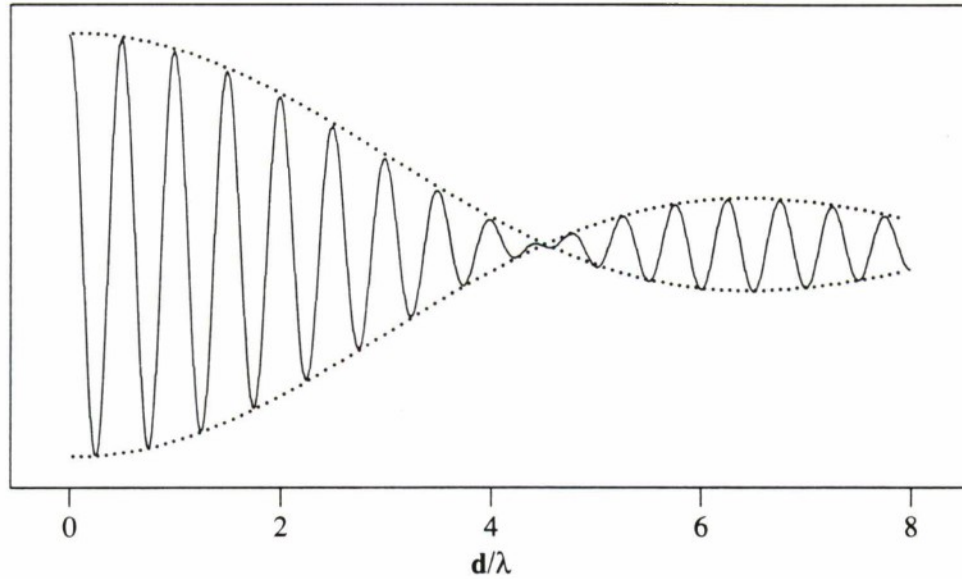


Figure 3.2. Typical fringe pattern with envelope.

### 3.3.2 Spatial Coherence

#### 3.3.2.1 Young's Experiment

Every real light source has some bandwidth, so the temporal coherence effects discussed above are important. In addition, every real source has some finite size, so the point source approximation is never completely valid. When we consider extended sources, we need to consider both spatial and temporal coherence.

In our discussion of temporal coherence, we considered the analytic signals  $u(P, t)$  and  $u(P, t + \tau)$ . For  $\tau$  smaller than the correlation time, the signals were correlated. In the case of spatial coherence we want to consider the analytic signals  $u(P_1, t)$  and  $u(P_2, t)$ . We expect that for point separations smaller than the correlation distance, the signals will be correlated.

It is possible to work with close approximations to point sources and get results in good agreement with the theory of the previous subsection. Such light has a spatial correlation function which is an impulse, e. g., its spatial frequency spectrum is white.

Unfortunately, it is not practical to obtain light which has an impulse for its time correlation function (white spectrum). Hence we are unable to study the effects of spatial correlation in isolation; we must consider spatial and temporal correlation together.

The canonical experiment in spatial and temporal correlation was performed by Thomas Young. As shown in Figure 3.3, light from an extended source passes through two pinholes and then forms an interference pattern on a viewing screen.

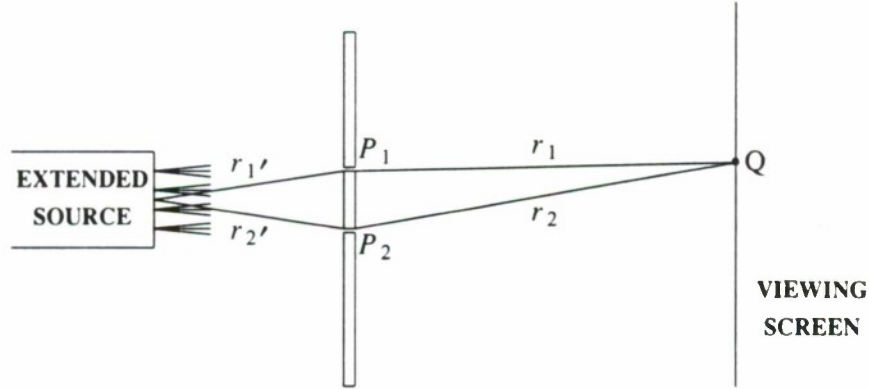


Figure 3.3. Young's interference experiment.

If we assume that the time delay difference  $(r_2 - r_1)/c$  is much less than the coherence time of the light source, interference fringes will appear on the viewing screen. The depth of modulation will depend on the degree of correlation between the light waves from the two points. We express the intensity at point Q as

$$I(Q) = \langle \mathbf{u}^*(Q, t) \mathbf{u}(Q, t) \rangle. \quad (3.9)$$

### 3.3.2.2 Narrowband Case

If the light is narrowband, and the pinholes are not too large, we can write the analytic signal at Q in terms of the signals at  $P_1$  and  $P_2$

$$\mathbf{u}(Q, t) = K_1 \mathbf{u}(P_1, t - r_1/c) + K_2 \mathbf{u}(P_2, t - r_2/c). \quad (3.10)$$

We can employ Equation (3.4) to perform the unusual feat of integrating over pinholes and find that

$$K_i \approx \iint_{P_i} \frac{\xi(\theta_i)}{j\lambda r_i} dS_i, \quad i = 1, 2. \quad (3.11)$$

It is not our purpose to impart great insight into the results of Young's experiment and all the possible fringe patterns that result, but we do want to see how even in such a simple experiment certain multi-dimensional quantities appear. It will be important for our later analysis to understand the basic definitions and units of some of these quantities.

To that end, define

$$I^{(i)}(Q) \equiv |K_i|^2 \langle |\mathbf{u}(P_i, t - r_i/c)|^2 \rangle, \quad i = 1, 2 \quad (3.12)$$

the individual intensities and

$$\Gamma_{12}(\tau) \equiv \langle \mathbf{u}(P_1, t + \tau) \mathbf{u}^*(P_2, t) \rangle \quad (3.13)$$

the *mutual coherence function*. Substituting these expressions into Equations (3.10) and (3.9), and noting that the  $K_i$  are purely imaginary, we obtain

$$I(Q) = I^{(1)}(Q) + I^{(2)}(Q) + 2K \operatorname{Re}[\Gamma_{12}(\frac{r_2 - r_1}{c})] \quad (3.14)$$

where

$$K \equiv K_1 K_2^* + K_1^* K_2. \quad (3.15)$$

We are studying the intensity of an optical wave, which has units of power. We have decomposed the intensity resulting from Young's experiment into three parts: the intensities contributed by the diffraction patterns of the first and second pinholes and the intensity resulting from mutual coherence. The actual pattern of intensity is rather complicated and reflects both temporal and spatial coherence.

Since the pinholes are small, the diffraction patterns are essentially constant. Hence they contribute a constant background upon which is superimposed a fringe pattern with slowly varying envelope and phase. Where the path length difference is zero or small, the fringe pattern is primarily attributable to temporal coherence effects. When the path length difference becomes large, the shrinking of the fringe envelope is primarily attributable to spatial coherence effects.

### 3.3.2.3 Quasi-monochromatic Case

We want to consider an even more special case in this subsection. In addition to the narrowband assumption in which  $\Delta\nu \ll \bar{\nu}$  we will here assume that the coherence length  $\tau_c$  of the light is much greater than the maximum path length difference. Referring to Figure 3.3,

$$\frac{|(r_1 + r_1') - (r_2 + r_2')|}{c} \ll \tau_c. \quad (3.16)$$

With this assumption, the fringe contrast is constant over the observation region of interest and the mutual coherence function can be written as

$$\Gamma_{12}(\tau) = J_{12} e^{-j2\pi\bar{\nu}\tau} \quad (3.17)$$

where  $J_{12} \equiv \Gamma_{12}(0)$  is the *mutual intensity* of the light at pinholes  $P_1$  and  $P_2$ . In this formulation,  $J_{12}$  is the phasor amplitude of a constant spatial sinusoidal fringe across the observation region.

### 3.3.3 Propagation of Mutual Coherence

As an optical wave propagates through space, its detailed structure changes. Similarly, its mutual coherence function changes, so we can say that mutual coherence "propagates." Things get a little more complicated when we consider the mathematical representation of propagation of mutual coherence.

As can be seen with reference to Figure 3.4, the dimensionality of the functions increases. Instead of two pinholes  $P_1$  and  $P_2$ , we have two sets of points  $P_i$  and  $Q_i$ . We assume that we know the mutual coherence function  $\Gamma(P_1, P_2; \tau)$  on the surface  $\Sigma_1$ , that is, we know the results of Young's interference experiment for all possible pairs of pinholes  $P_i$ . We wish to use this information to determine the mutual coherence function  $\Gamma(Q_1, Q_2; \tau)$  on the surface  $\Sigma_2$ , that is, predict the results of Young's interference experiment for all possible pairs of pinholes  $Q_i$ .



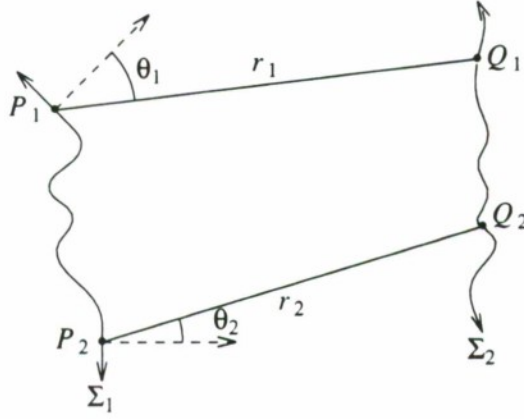


Figure 3.4. Mutual coherence propagation geometry.

Modifying our notation slightly, in Equation (3.13) we defined the mutual coherence function on  $\Sigma_2$  as

$$\Gamma(Q_1, Q_2; \tau) = \langle \mathbf{u}(Q_1, t + \tau) \mathbf{u}^*(Q_2, t) \rangle. \quad (3.18)$$

We can use Equation (3.4) to express the fields on  $\Sigma_2$  in terms of the fields on  $\Sigma_1$  in the case of narrowband light:

$$\begin{aligned} \mathbf{u}(Q_1, t + \tau) &= \iint_{\Sigma_1} \frac{\mathbf{u}(P_1, t + \tau - r_1/c)}{j\tilde{\lambda}r_1} \chi(\theta_1) dS_1 \\ \mathbf{u}^*(Q_2, t) &= \iint_{\Sigma_1} \frac{-\mathbf{u}^*(P_2, t - r_2/c)}{j\tilde{\lambda}r_2} \chi(\theta_2) dS_2 \end{aligned} \quad (3.19)$$

Substituting (3.19) into (3.18), with a little manipulation and another application of (3.19) we obtain the moderately formidable

$$\Gamma(A_1, Q_2; \tau) = \iint_{\Sigma_1} \iint_{\Sigma_1} \iint \Gamma(P_1, P_2; \tau + \frac{r_2 - r_1}{c}) \frac{\chi(\theta_1)}{\tilde{\lambda}r_1} \frac{\chi(\theta_2)}{\tilde{\lambda}r_2} dS_1 dS_2. \quad (3.20)$$

We will not need to spend any time contemplating the inner nature of quadruple integrals; we will immediately specialize the result and get things to more manageable proportions. Our goal is to provide background helpful in understanding the important Van Cittert-Zernike theorem, and we are almost there.

### 3.3.4 Propagation of Mutual Intensity

If the quasi-monochromatic condition of Equation (3.16) is satisfied the mutual intensity

$$\mathbf{J}(Q_1, Q_2) = \Gamma(Q_1, Q_2; 0) \quad (3.21)$$

is of interest. Applying Equation (3.17) to Equation (3.20), we obtain

$$\mathbf{J}(Q_1, Q_2) = \iint_{\Sigma_1} \iint_{\Sigma_1} \mathbf{J}(P_1, P_2) e^{\frac{-j2\pi(r_2 - r_1)}{\bar{\lambda}}} \frac{\chi(\theta_1)}{\bar{\lambda}r_1} \frac{\chi(\theta_2)}{\bar{\lambda}r_2} dS_1 dS_2, \quad (3.22)$$

the propagation law for mutual intensity. The intensity distribution on the surface  $\Sigma_2$  is obtained by letting  $Q_1 \rightarrow Q_2$  in Equation (3.22).

### 3.4 THE VAN CITTERT-ZERNIKE THEOREM

#### 3.4.1 Coherent and Incoherent Sources

We will next briefly discuss coherent and incoherent wavefields. It seems logical to call optical waveforms at points  $P_1$  and  $P_2$  subject to time delay  $\tau$  fully coherent if the magnitude of the normalized coherence function is unity

$$|\gamma_{12}(\tau)| = 1 \quad (3.23)$$

where

$$\gamma_{12} \equiv \frac{\Gamma_{12}(\tau)}{\sqrt{\Gamma_{11}(0)\Gamma_{22}(0)}}. \quad (3.24)$$

$\gamma$  ranges from 0 to 1 in the same way as a correlation coefficient. Since only monochromatic waves satisfy (3.23), it has been found useful to call a wavefield fully coherent if, for every pair of points  $P_1$  and  $P_2$ , there exists some delay  $\tau$  such that Equation (3.24) is satisfied.

Similarly, it seems logical to define an incoherent field by requiring

$$|\Gamma_{12}(\tau)| = 0 \quad P_1 \neq P_2 \quad (3.25)$$

but this definition is even less useful than the first attempt at defining fully coherent wavefronts since it does not allow any propagation at all! Essentially it describes a nonradiating source. The closest we can come to incoherence with a radiating wave turns out to be a fairly messy expression involving Bessel functions. However, in practice as long as the optical system resolution is much less than  $\bar{\lambda}$ , we can approximate the mutual intensity of an incoherent source by

$$\mathbf{J}(P_1, P_2) = \frac{\bar{\lambda}^2}{\pi} I(P_1) \delta(\Delta x, \Delta y) \quad (3.26)$$

where  $\delta(.,.)$  is a two-dimensional Dirac delta function and  $\Delta x$  and  $\Delta y$  are the differences in the  $x$  and  $y$  coordinates of points  $P_1$  and  $P_2$ .

#### 3.4.2 Outline of Mathematical Derivation

The Van Cittert-Zernike theorem describes the mutual intensity function produced by an incoherent source. Such sources are of primary concern to us in the passive surveillance situation, as discussed previously. If we start with Equation (3.22), the propagation law, and substitute in Equation (3.26) for the mutual intensity, we nicely simplify things to

$$\mathbf{J}(Q_1, Q_2) = \frac{1}{\pi} \iint_{\Sigma} \mathbf{I}(P_1) e^{\frac{-j 2\pi(r_2 - r_1)}{\bar{\lambda}}} \frac{\chi(\theta_1)}{\bar{\lambda} r_1} \frac{\chi(\theta_2)}{\bar{\lambda} r_2} dS \quad (3.27)$$

where  $\Sigma$  is the source.

This result is useful for quasi-monochromatic incoherent sources only, but we need to specialize it still further. Assume that the distance  $z$  between the source and the observation region is much greater than the size of either of them. Then  $r_1 r_2 \approx z^2$ , and since the angles are small,  $\chi(\theta_i) \approx 1$ . We then obtain the simplification

$$\mathbf{J}(Q_1, Q_2) = \frac{1}{\pi z^2} \iint_{\Sigma} \mathbf{I}(P_1) e^{\frac{-j 2\pi(r_2 - r_1)}{\bar{\lambda}}} dS. \quad (3.28)$$

To define the coordinate systems, let the source and observation planes be separated in the  $z$  dimension, let the perpendicular coordinates in the observation plane be  $(x, y)$ , and let the coordinates in the source plane be  $(\xi, \eta)$ . Substituting these coordinates for the  $r_i$  and using the approximations, with a little manipulation we arrive at the expression

$$\mathbf{J}(x_1, y_1; x_2, y_2) = \frac{e^{-j\psi}}{\pi z^2} \iint_{\Sigma} \mathbf{I}(\xi, \eta) \frac{e^{-j 2\pi(\Delta x \xi + \Delta y \eta)}}{\bar{\lambda}} dS \quad (3.29)$$

where the phase factor  $\psi$  is given by

$$\psi = \frac{\pi}{\bar{\lambda} z} \left[ (x_2^2 + y_2^2) - (x_1^2 + y_1^2) \right]. \quad (3.30)$$

In words, the mutual intensity function at the observation plane is the two-dimensional Fourier transform of the source intensity multiplied by a phase factor. There are conditions under which the phase factor is approximately unity and may be omitted. In our situation, we will not need to worry about this factor.

Note that mutual intensity is more general than image intensity; when discussing the latter,  $\mathbf{J}(x_1, y_1; x_2, y_2)$  becomes simply  $\mathbf{J}(x, y)$  as the two points converge to one.

### 3.5 PROPAGATION THROUGH TRANSMITTING OBJECTS

Goodman<sup>4</sup> presents the general theory which enables one to compute image intensity when partially coherent light is transmitted through objects. It is then easy to consider the special cases of total coherence and incoherence. Since things get rather complicated and we do not need to consider coherent sources, we will just present the results we need without summarizing any of the proofs.

We will first describe the intensity Fourier transform property of lenses. This will provide the mathematical framework for understanding imaging with incoherent light. We will then define the optical transfer function. This will be important in characterizing the atmosphere.

### 3.5.1 The Effect of a Lens on Image Intensity

It is well known that a lens acts as a Fourier transformer for coherent light; the complex fields in the focal planes are a Fourier transform pair. We, however, are concerned with incoherent light, which leads us to consider the propagation of mutual coherence through a lens.

If we restrict ourselves to quasi-monochromatic light, it can be shown that the mutual intensity functions in the focal planes of a thin positive lens are a four-dimensional Fourier transform pair. We are most interested in the intensity in the back focal plane which results from an incoherent source in the front focal plane. In this case, both functions reduce from four dimensions to two and we have a two-dimensional Fourier transform relationship.

We will not be studying this derivation or performing any calculations with it, so we will not show the relevant equations. The theorem we wish to remember is simply that when we have quasi-monochromatic incoherent light at the front focal plane of a thin lens, the intensity distribution in the back focal plane is the two-dimensional Fourier transform of the source mutual intensity.

This theorem complements the Van Cittert-Zernike theorem discussed above. Assume an astronomical object at a great distance is illuminated by (or emits) incoherent light which is either inherently quasi-monochromatic or is later filtered to satisfy this condition. By Van Cittert-Zernike the mutual intensity is the Fourier transform of the source intensity. If the light then enters a suitable lens, the back focal plane intensity will be the Fourier transform of the mutual intensity. Since the Fourier transform and the inverse Fourier transform differ only in scale factor and phase, we see an image of the source, which probably won't surprise anyone who believes in telescopes.

One missing factor in this scenario is the atmosphere, which degrades the image so that it is *not* a replica of the source intensity distribution. In addition, the finite size of the lens means that we are selecting a finite number of spatial frequencies, and hence there is a high-frequency cutoff determined by the size of the lens pupil.

### 3.5.2 The Optical Transfer Function

There are certain conditions under which a transmitting object can be characterized by an *optical transfer function* (OTF). Such an object could be a lens or other imaging system, the atmosphere, or some combination.

First, the illumination must be incoherent in the sense of Equation (3.26). We will find that an incoherent system is linear in intensity, while a coherent system is linear in complex amplitude.

The second requirement for the OTF to exist is that our system must be isoplanatic. The spatial analog of the stationarity property of time processes goes by a number of names, including shift-invariance, space-invariance, and isoplanaticity. By any name, it loosely means that the statistical properties of a random process do not depend on the spatial coordinates at which they are measured. In practice this is true if the object under examination does not subtend a very large angle.

Under these assumptions, and assuming quasi-monochromaticity, if we denote the object intensity distribution  $o(x,y)$  and the transmitting object point spread function (really, intensity spread function)  $t(x,y)$ , we find that the image intensity is

$$i(x,y) = o(x,y) * t(x,y). \quad (3.31)$$



This convolution relationship is a product in the frequency domain

$$I(u,v) = O(u,v) T(u,v). \quad (3.32)$$

Note that we have here departed from Goodman's notation, anticipating future discussions of speckle image processing.

Intuitively, when a distant object is imaged through the atmosphere, we apply first Van Cittert-Zernike and then the thin lens relationship. The atmosphere OTF  $O(u,v)$  is acting on the mutual intensity function, the Fourier transform of the source intensity. If we insist on considering things in the intensity domain, a convolution with the point spread function  $o(x,y)$  is necessary.

The OTF is a complex quantity; the magnitude of the OTF is known as the *modulation transfer function* (MTF) and will be important in our later discussions.

### 3.6 THE INTERFEROMETRIC VIEW OF IMAGING

Recall Young's experiment, in which light passes through two pinholes and forms an interference pattern on a viewing screen as in Figure 3.3. If the pinholes are moved close together, a one-wavelength path difference spans more distance on the screen, so the period of the interference pattern is large. Greater pinhole spacing produces interference patterns with smaller period or higher spatial frequency. The pinholes are taken to be small compared to the coherence distance of the light source.

The exit pupil of an imaging system can be assumed to be composed of many pinholes.<sup>6,4</sup> Each possible pair of these imaginary pinholes generates an interference pattern, and we can consider the whole image to be built up of a number of sinusoidal fringes. The spatial frequencies  $v_u$  and  $v_v$  are related to the pinhole separations  $\Delta x$  and  $\Delta y$  by

$$\begin{aligned} \Delta x &= \lambda z v_u \\ \Delta y &= \lambda z v_v. \end{aligned} \quad (3.33)$$

If the object is at a great distance  $z$  it is convenient to divide both sides of these equations by  $z$ , expressing the separation in radians rather than meters and the spatial frequencies in cycles/rad rather than cycles/m.

The amplitude and phase of the fringe pattern from a given pair of pinholes located at  $(x_1, y_1)$  and  $(x_2, y_2)$  are determined by the amplitude and phase of the mutual intensity leaving the exit pupil  $J_p(x_1, y_1; x_2, y_2)$ . Since there are many pinhole pairs with any given spacing, the resultant fringe pattern at a given spatial frequency is calculated by summing over all such pairs. If the optics are perfect, and assuming incoherent illumination and Van Cittert-Zernike, the mutual intensity is of the form  $J_p(\Delta x, \Delta y)$  and all pinhole pairs with a given spacing add coherently to form the image.

Consider the transfer function of an ideal circular lens. It is easy to see that the higher spatial frequencies, corresponding to greater point spacings, are attenuated relative to the lower frequencies, since there are fewer point pairs in the aperture with large spacings. At left in Figure 3.5 are representative point pairs with identical spacing. The number of such pairs relative to the number of pairs with zero spacing is given by the shaded area in the right diagram divided by the total aperture size. This is mathematically an autocorrelation of the circular lens pupil.

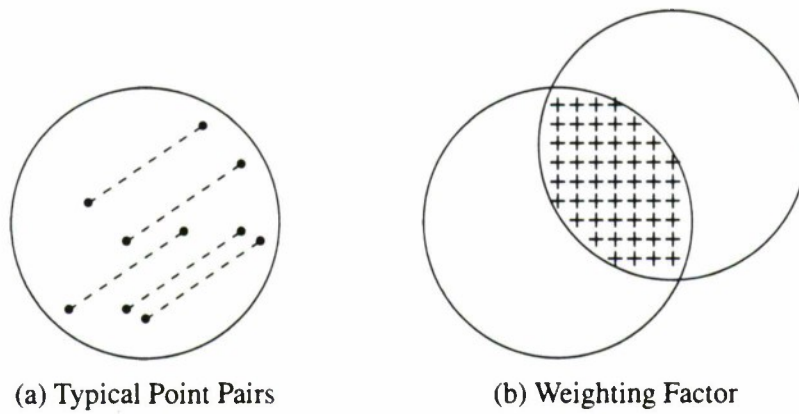


*Figure 3.5. Interferometric imaging model.*

## 4. ATMOSPHERIC TURBULENCE

### 4.1 INTRODUCTION

The general theory of light propagation through atmospheric turbulence was introduced in the important book by Tatarski.<sup>7</sup> This translation from the Russian drew on a lot of Russian work and has been the basis for most of the work in this area since. The mathematics is not simple, so we will again adopt the approach of outlining the important results in an effort to gain intuitive understanding.

After Tatarski, we wish to discuss briefly the papers of Hufnagel and Stanley<sup>8</sup> and Fried.<sup>9</sup> Another major step in this area was made by Korff<sup>10</sup> but we will consider it in our discussion of speckle imaging since it arose in that context. All these authors rely on the approach of Tatarski, and use similar notation. We will describe the assumptions made by Tatarski and his successors about the atmosphere, as well as the effect of those models on the amplitude and phase of transmitted light. We will later apply these results to the analysis of adaptive optics and speckle imaging.

Not all of Tatarski's assumptions seem transparent on first reading; in particular it is sometimes hard to determine typical ranges of certain parameters. Goodman<sup>4</sup> puts Tatarski's work in slightly more modern context and is recommended as an introduction.

### 4.2 STATISTICAL REPRESENTATION OF ATMOSPHERIC PARAMETERS

#### 4.2.1 Structure Functions

It is convenient when dealing with stationary random functions to use the mean, the autocorrelation function  $R(\tau)$ , and the spectral density  $S(f)$ , the latter two being of course a Fourier transform pair. When a process is nonstationary, we must work with the more general mean, a function of time, and the more general autocorrelation function  $R(t, s)$ .

In meteorology, we often deal with quantities which are nonstationary such as air pressure and temperature. About 50 years ago Kolmogorov introduced a means of mathematically separating very slow variation in the mean from the more rapid variation for any random process. Instead of using the absolute value of some parameter  $f(t)$  he considered the incremental changes

$$F_\tau(t) \equiv f(t + \tau) - f(t). \quad (4.1)$$

It is intuitively obvious that if  $\tau$  is chosen appropriately, we may end up with an essentially stationary process  $F_\tau$  which reflects all fluctuations whose period is less than  $\tau$ .

The next obvious step is to consider the autocorrelation function of the process  $F_\tau$ . It turns out, however, as discussed in Appendix B, that this autocorrelation function can be expressed in terms of so-called structure function  $D_f(t_i, t_j)$ . If the structure function may be represented in the form

$$D_f(\tau) \equiv \overline{[f(t + \tau) - f(t)]^2} \quad (4.2)$$

we say that the process has stationary increments. This is the model of interest to us.



#### 4.2.2 Random Fields

The multi-dimensional analog of the random process is called a random field. Notationally, following Tatarski, in the three-dimensional case define the vector  $\vec{r}_i \equiv (\vec{x}_i, \vec{y}_i, \vec{z}_i)$ . The spatial autocorrelation function of a random field takes the general form  $R(\vec{r}_1, \vec{r}_2)$ . If the random field is homogeneous and isotropic, this may be written as  $R(|\vec{r}_1 - \vec{r}_2|)$ . In this latter case, things reduce to a single dimension; in particular, the spectral density exists as a function of one variable.

It may seem like quite a simplification to model the atmosphere as homogeneous and isotropic. In fact, the large scale effects which cause slow variation in means of atmospheric parameters also result in inhomogeneities and anisotropy. The solution is the same; the use of structure functions enables us to obtain approximately homogeneous, isotropic, stationary random fields.

#### 4.3 PHYSICS OF TURBULENCE

Turbulence exists on a wide range of scales. The smallest of these is in the range of several millimeters, and the largest is on the order of tens of meters. Kolmogorov denoted these the “inner” and “outer” scales of the turbulence.

The atmospheric quantity of most interest to us is the refractive index. This depends on temperature, pressure, and wavelength, but the fluctuations depend mostly on temperature. Define the wavenumber vector  $\vec{\kappa} \equiv (\kappa_x, \kappa_y, \kappa_z)$ , a vector frequency measured in radians per meter. In the isotropic case we can work with  $\kappa \equiv \sqrt{\kappa_x^2 + \kappa_y^2 + \kappa_z^2}$ . For  $\kappa$  consistent with the two turbulence scales mentioned above Kolmogorov gave the form of the power spectral density of refractive fluctuations

$$\Phi_n(\kappa) = 0.033 C_n^2 \kappa^{-11/3}. \quad (4.3)$$

In this expression,  $C_n^2$  is called the *structure constant* of the refractive index fluctuations. When we couch things in terms of structure functions,

$$D_n(r) = C_n^2 r^{2/3}. \quad (4.4)$$

The numerical value of  $C_n^2$  ranges from  $10^{-13}$  to  $10^{-17} \text{ m}^{-2/3}$ .

Kolmogorov’s work is rather old, but like politicians it is easier to criticize than to replace. One new area of study which is relevant to turbulence is the area of nonlinear dynamics, often called chaos theory.<sup>11</sup> Kolmogorov was aware that the above expression is not applicable when energy dissipation becomes too significant (for small scale sizes) but more is understood about the phenomenon today. Clearly there is merit to Kolmogorov’s work since it is supported by experiment to useful extent, but future advances may give us more accurate analyses.

#### 4.4 OPTICAL PROPAGATION THROUGH TURBULENCE

##### 4.4.1 Amplitude and Phase Fluctuations

It is beyond the scope of this report to reproduce much of Tatarski’s analysis of optical propagation through turbulence. We will not consider Maxwell’s equations or a host of other relationships and approximations which are relevant. Our goal is just to present the end results, with as much physical meaning as possible.



Tatarski moves through a series of successive analyses of progressively more realistic scenarios. Although it might build character for us to recapitulate some of this, we will instead skip to the most relevant case. Here we assume that the structure constant  $C_n^2$  varies slowly, with significant changes only occurring for path lengths on the order of the outer scale of turbulence.

We will present expressions for the log-amplitude and phase of the fluctuation. There are a couple of reasons why we consider the log-amplitude rather than just the amplitude, but suffice it to say here that for weak fluctuations (good seeing) experiment suggests that amplitude fluctuations are log-normally distributed. Equivalently, the log-amplitude is normally distributed. Hence the log-amplitude is the natural quantity of interest.

Notationally, let the refractive index be represented as

$$n(\vec{r}) = n_0(\vec{r}) + n_1(\vec{r}) \quad (4.5)$$

where the constant term  $n_0(\vec{r}) \approx 1$  and the fluctuating term  $n_1(\vec{r}) \ll 1$ . Let the phase of the wave be  $S \equiv S_0 + S_1$  and the amplitude  $A$  satisfy  $\log A = \log A_0 + \chi$ . Tatarski gives an expression for the log-amplitude fluctuations

$$\overline{\chi^2} = K_\chi \int_0^L C_n^2(\vec{r}) x^2 dx. \quad (4.6)$$

We won't worry about the constant  $K_\chi$ , since we won't be doing any numerical calculations with this expression.

The phase of the fluctuation is generally assumed normally distributed. Rather than considering the fluctuations directly, Tatarski derives an expression for the structure function of the phase

$$D_S(\rho) = K_S \rho^{5/3} \int_0^L C_n^2(\vec{r}) dx. \quad (4.7)$$

Again, the exact value of the constant is not of interest.

To interpret Equations (4.6) and (4.7), consider the following facts. First, amplitude fluctuations are much less significant than phase fluctuations; indeed adaptive optics and speckle imaging would not work in their present forms if this was not the case. Second, since the density of air decreases so rapidly with elevation, refractive index changes tend to be greatest near the ground.

Looking at Equation (4.7), we see that we are integrating  $C_n^2$  from the ground up. We expect that the turbulence near the ground is the major contributor to the phase fluctuations. On the other hand, Equation (4.6) weights the integral contributions by the square of the altitude. Hence we expect the higher layers of turbulence to make the major contribution to amplitude fluctuation.

The integral-weighting situation should tend to reduce the correlation between amplitude and phase fluctuations. In other words, the instantaneous mathematical correlation of these fluctuations should be low because they arise from largely different physical sources of turbulence, different air masses. Incidentally, Fried<sup>9</sup> argues that the difference processes for phase and amplitude are uncorrelated due to isotropy. Since they are Gaussian, it follows that they are independent. This is not exactly the same point we are making here.

It is quite possible for amplitude and phase fluctuations to be highly correlated in the rms (average) sense, e. g., periods of large phase fluctuation corresponding to large amplitude fluctuation. The issue is whether or not the turbulent activity in the lower layers generally tracks the turbulence in the upper layers. If so, devices which measure amplitude fluctuations such as stellar scintillation should be useful for characterizing phase fluctuations most of the time. If not, we may notice discrepancies when we characterize the atmosphere with a scintillometer in an effort to predict the performance of devices which correct phase.

#### 4.4.2 Fried's Parameter

In 1964 Hufnagel and Stanley<sup>8</sup> built on Tatarski's foundation by considering the long-term average MTF of turbulence. Their method involved calculating average mutual coherence functions. Fried<sup>9</sup> followed with a more important paper calculating both long-term and short-term average MTFs. He showed that there is much less high spatial frequency attenuation in the short-term case. In addition, he introduced a new parameter for characterization of turbulence.

Briefly, the mutual coherence function of the wavefront after passing through turbulence is central to the analysis. This turns out to be what Fried calls the wave-structure function

$$D(\vec{r}) \equiv D_\chi(\vec{r}) + D_S(\vec{r}). \quad (4.8)$$

This quantity had previously popped up in Tatarski's work in the derivation of  $D_S(\vec{r})$  and is given by

$$D(\vec{r}) = A \vec{r}^{5/3}. \quad (4.9)$$

Fried defined a new constant

$$r_o \equiv \left[ \frac{6.88}{A} \right]^{3/5} \quad (4.10)$$

which lets us write

$$D(\vec{r}) = 6.88 \left[ \frac{r}{r_o} \right]^{5/3}. \quad (4.11)$$

The advantage of characterizing turbulence using  $r_o$  instead of  $A$  is the physical picture in which turbulence converts the effective resolution of a large telescope into the resolution of a much smaller telescope.  $r_o$  is the diameter of that smaller telescope, e. g., a diffraction-limited telescope of diameter  $r_o$  gives resolution comparable to a very large telescope through the given turbulence.

Since Fried's work,  $r_o$  has become a standard measure of atmospheric turbulence or quality of astronomical seeing. It is a useful and easily understood single quantity, but of course it falls short of completely describing the three-dimensional atmosphere. One should also keep in mind that the use of  $r_o$  assumes isoplanicity, and attempts to image over excessive angles will violate this condition.

#### 4.5 SUMMARY

When Silverman translated Tatarski's book in 1961, a major contribution to the mathematical analysis of turbulence became accessible to the English speaking world. This approach was rapidly adopted

by many investigators, and optical propagation through turbulence achieved a much firmer mathematical basis, although the mathematical difficulties involved in exactly calculating some of the functions of interest were, and are, formidable.

Fried showed that the high spatial frequency transmission through turbulence was greatly attenuated by taking long term averages of received intensity, which explained some anomalous results of imaging experiments. In the short term case, there were different effects for the near-field and far-field cases, but in the long term case this distinction did not exist. Accordingly, Fried suggested that propagation be studied using long exposures so that the results could be better understood. He did hold out the hope that short exposures could be more useful after theory advanced.

Labeyrie<sup>3</sup> was the first to show how short exposures could be used to extract information from the higher spatial frequencies. The experimental protocols which followed were able to sidestep theoretical understanding of turbulence somewhat. Long-term averages of quantities derived from short exposures tended to reduce the need for understanding instantaneous turbulence. Measuring the effect of turbulence by observing stars enabled corrections to be made without any understanding of the underlying phenomenology. Experimentalists plunged into areas which were thought on theoretical grounds to be quicksand, sometimes surprising the experts.

We will consider these issues in detail below, but first we will consider the interesting and relatively hardware-intensive subject of adaptive optics. While speckle imaging is perhaps superior to adaptive optics for dim astronomical objects, we will find that some earth-orbiting satellites may be more easily imaged adaptively. Considering speckle imaging and adaptive optics together will suggest interesting combinations of these techniques.



## 5. ADAPTIVE OPTICS

### 5.1 OVERVIEW

Adaptive or active optics describes any system in which the optical components change configuration during operation. Historically, due to the small wavelengths involved, most man-made optical devices were rigid lenses and mirrors made out of a material like glass. Such devices operate in an "open loop" manner with fixed configuration unaffected by equipment operation.

Biological imaging systems have not been bound by such constraints; the human eye is able to adjust its focus by changing the shape of the lens, maintaining focus on moving objects. Another familiar example of adaptive optics is a camera with automatic focusing. Here the adaptation is performed by moving rigid lenses. In both cases a feedback control system operates to minimize deviation from desired performance.

There are other examples of applications in which relatively slow adaptation is effective, and in which the degradation can be characterized by a small number of parameters. Large space-based optics will require some adaptation to maintain their configuration in the presence of nonuniform solar heating. Large land-based telescopes<sup>12</sup> constructed of many smaller mirrors will use adaptive methods to reduce required rigidity and weight while decreasing optical errors.

The most challenging case is adapting to rapidly varying optical disturbances which are themselves complex in nature, as in the important problem of atmospheric turbulence. This was first achieved about 15 years ago and is our primary concern. We will henceforth use the terminology *adaptive optics* to refer to such systems. Hardy<sup>1</sup> has written an excellent summary of the area as of about 1978. Most of it is still highly relevant, although of course there have been certain advances since that time.

We can divide adaptive optics systems into two categories, active and passive. The active is concerned with transmitting energy, typically produced by a laser, through turbulence. The beam is pre-compensated to largely cancel the effects of the turbulence. The passive system corrects the received wavefront to cancel turbulence. We will say no more about active systems.

There are two basic approaches to passive adaptive optics, illustrated in Figure 5.1. In the *wavefront compensation* approach, a wavefront modifier attempts to compensate for the effects of atmospheric turbulence. After modification by this device, the wavefront is split so that part of the energy is used to make an image and the rest is sent to a wavefront detector. The latter device maps out the residual wavefront deviation, which is then converted to modifier control signals by the processor. These signals are added to the existing ones and the closed-loop system attempts to null the error.

In the *image sharpening* approach deliberate distortions are introduced in the received wavefront over a wide variety of amplitudes and shapes. The intensity detector determines which of the trial modifications introduced by the aperture tagger is effective in improving image "sharpness." The processor converts that information into control signals which add an appropriate modification to the wavefront through the wavefront modifier.

The most successful approach to date has been the wavefront compensation one, which we will henceforth refer to as *compensated imaging*, and we will spend most of our time discussing it. The



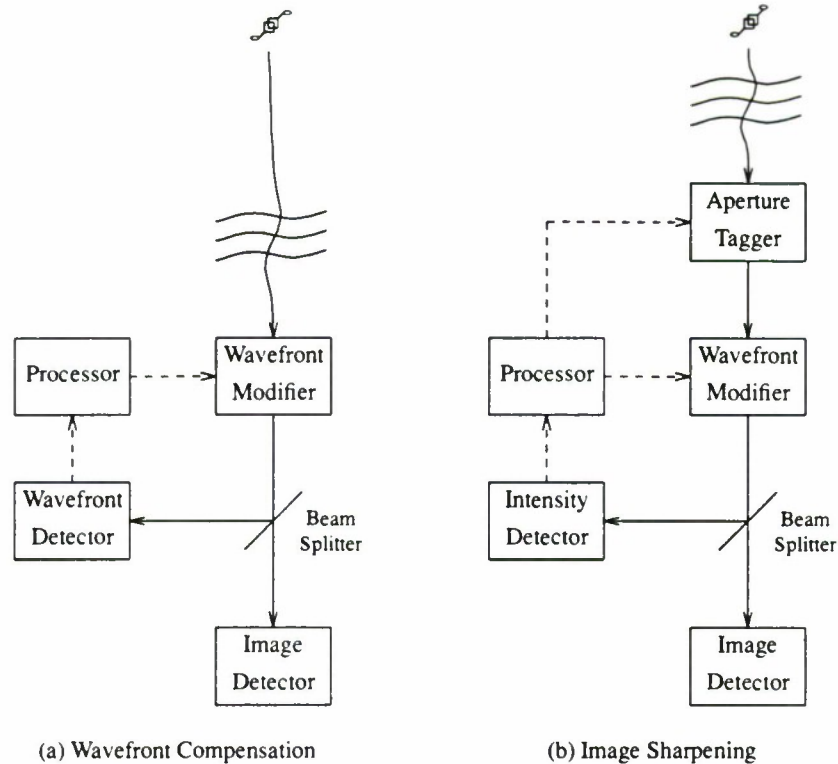


*Figure 5.1. Adaptive optics systems.*

image sharpening work is important in some applications such as solar imaging where compensated imaging is inappropriate. More importantly, the reported work on image sharpening will influence our analysis of compensated image restoration. It will also be of interest in our discussion of speckle imaging of satellites.

## 5.2 HISTORY

In the early 1970s DARPA funded experimental investigations into compensated imaging by Hardy and his colleagues at Itek. In late 1973 a practical compensated imaging device<sup>2</sup> was demonstrated. We will briefly summarize the configuration of this device here; we will describe the components in more detail below.

A 30 cm aperture was divided into 21 subapertures. The wavefront modifying device was a monolithic piezoelectric mirror (MPM). The MPM itself was not as large as 30 cm; the light was collimated by a lens before striking the smaller MPM. The wavefront detector was an array of interferometers, which produced 32 wavefront tilt measurements, 16 in each of two orthogonal directions. An analog computer solved the least squares problem of converting the 32 available measurements into the best deflection for each of the 21 MPM actuators. In addition, a separate system processed the wavefront sensing data and corrected overall waveform tilt. This was a great step forward, and required advances in almost every component to work successfully.

The next milestone was a 69 subaperture MPM-based system built by Hardy at Itek Corporation for Division 5 of Lincoln Laboratory. A 60 cm aperture was used, so the subapertures were slightly larger than in Hardy's original design. The same type of interferometer was used for phase sensing, although its wavelength insensitivity was not needed for this laser application. This appears to be very much a scaled-up version of its predecessor. The only apparent improvement besides the increased size is the replacement of the analog phase-lock-loop phase measurement circuitry by digital correlation equipment.

The next step in the progression is an imaging system<sup>13</sup> known as the Compensated Imaging System (CIS), which was put into service in Hawaii in 1981. This device was again built by Itek, using essentially the same technology as its predecessors, but with a 1.6 m aperture. The CIS is operated by AVCO as part of AMOS/MOTIF (ARPA Maui Optical Station/Maui Optical Tracking and Identification Facility). This is a large and impressive piece of equipment; it is currently the logical choice for experiments in adaptive optical space surveillance.

The astronomy community has not been able to afford compensated imaging equipment for the most part. The expense and the limitation to bright objects has made the payoff look less than the payout. There is a potential program<sup>14</sup> of interest being promoted by the NOAO organization. This would perform adaptive correction in the infrared, the reasoning being that a large aperture requires many fewer subapertures due to the increase in  $r_o$  in the infrared.

The data which might be produced by such a system are not of as much interest as the theoretical papers written by the university astronomers involved in the project. It seems that when you are knee-deep in data from a real system, you spend most of your time looking at lists of satellites and sending videotapes to sponsors. The astronomers, on the other hand, lacking data from any operational system, are forced to analyze their projected system in meticulous detail to minimize risk and cost. Where theory fails, they usually have access to computers suitable for simulation. We will reference some of their work when we discuss errors in adaptive systems.

Departing from the mainstream of compensated imaging, Muller and Buffington published some results<sup>15</sup> on image sharpening at the same time that Itek was working on the initial prototype of their equipment. They showed that the integral of the squared image intensity is a suitable sharpness measure for controlling adaptive optics. They considered other measures as well, reporting the results of computer simulations. Later Buffington *et al*<sup>16,17</sup> described experiments with real hardware.

### 5.3 MPM DESCRIPTION

The monolithic piezoelectric mirror (MPM) is the most successful wavefront modifying device to date. Hardy *et al*<sup>2</sup> describe a 21-element MPM in detail. This device consists of a monolithic cylinder of sintered lead-zirconate-titanate (PZT), a standard piezoelectric material. The dimensions are about 5 cm diameter and 1.2 cm thick.

An array of electrodes is placed on the top of the PZT, addressed by wires passing through to the back. A common electrode covers the back surface and a mirror is glued to the front surface.

When a positive or negative voltage is applied to an electrode, a small localized region of the mirror deflects in the corresponding direction. There is reported to be little interaction between electrodes, a major advantage of this type of wavefront corrector.

One disadvantage is the high voltage required to operate the MPM; 2-4 kV to deflect the required 2000 nm or so. The inherent frequency response of the material is from dc to over 10 kHz, but the arrangement of amplifiers used in this original compensated imaging system reduced that to about 1 kHz. This does not represent any technology limitation today.

## 5.4 WAVEFRONT SENSOR DESCRIPTION

One of the problems with compensated imaging is that it requires enough light in each subaperture to estimate wavefront distortion. If the interferometers required filters to produce narrowband light, the situation would be exacerbated. Hence practical interferometers for this application operate with white light.

If we imagine the apparatus required for Young's experiment, we will be totally unprepared for the variety and complexity of modern interferometers. Rather than delve into the general subject, we will confine our discussion to the ac shearing interferometers used in the series of Itek interferometers and described by Hardy<sup>2,1</sup> and Koliopoulos.<sup>18</sup>

First we will be sure we understand just what we mean by wavefront "tilt." We assume that the effects of turbulence are continuous, so that optical path lengths do not vary significantly for very small spatial separations. In particular, the spatial path length function could be expanded in some small subaperture in a power series and represented by some constant plus the linear term, or actually one linear term for the x direction and one for y.

Now if we separate two pinholes in a Young's experiment by some small  $\Delta$  (a subaperture size), we will get an interference pattern which tells us the path difference, or equivalently the waveform tilt. A two-dimensional array of x and y tilts is really an expression of the differential path length function in terms of multiple truncated power series. If the subapertures are small enough, this is a highly accurate representation.

In fact, Young's experiment would tell us the phase difference of the incident narrowband light rather than the length difference. However, since the optical effects of turbulence are caused by variations in refractive index, the cause of the phase difference may be viewed as an underlying constant path length difference. Hence the phase difference will be proportional to frequency and white light interferometers can measure the distance, or, as in our case, the wavefront slope over the subaperture.

### 5.4.1 Hardy's Interferometer

We will now describe Hardy's variable-shear rotating ac interferometer, shown in Figure 5.2, which is about as complicated as its name. This device was developed especially for compensated imaging; in fact the first one was used in an upgrade of the original compensated imaging equipment.

Typically in a compensated imaging system, the light from the full aperture is collected and collimated into a much smaller diameter suitable for modification by the MPM. After MPM correction but before entering the final lens to be focused on the imaging system, the light is split into two paths, one for the x tilt measurement and one for the y tilt. Lens L1 focuses the light onto G, a rotating circular grating with alternating clear and opaque radial lines of equal thickness. A point of light projected anywhere on this grating produces a square wave time function on the other side. After diffraction by the grating, lens L2 forms multiple images of the wavefront on the detector array. When the aperture size



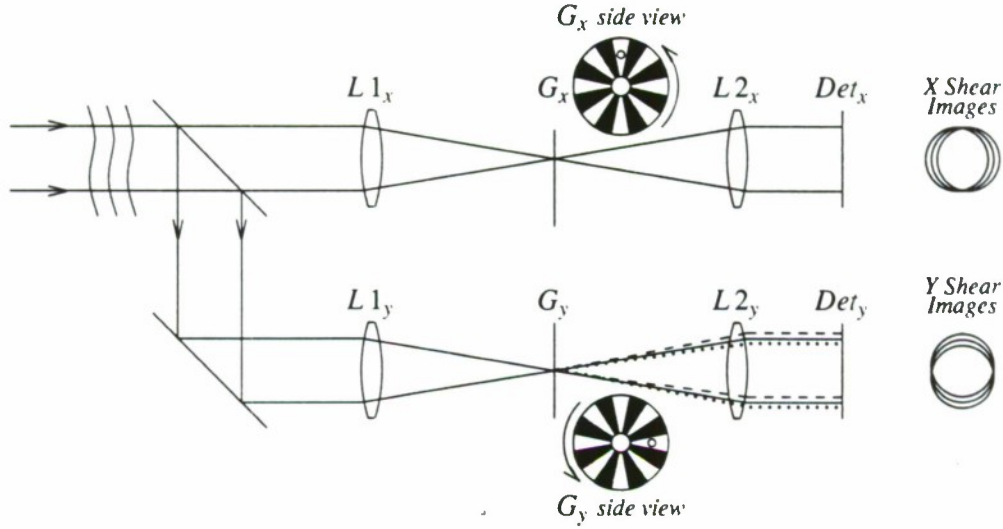


Figure 5.2. Variable-shear rotary ac interferometer.

(and number of subapertures) is increased, the detector array and associated electronics are the only things that need to be modified.

We can view the lens arrangement as an optical Fourier transformer; when we multiply the Fourier transform of the wavefront by a square wave that is the same as convolving the wavefront by an impulse train of odd harmonics. Not shown in Figure 5.2 is what happens after detection; the detector signals are processed by electrical filters which remove unwanted harmonics. Even though only three images are shown in Figure 5.2, there are practically an infinite number of them. Of course for a given shear (angular separation) only a finite number of them actually overlap in the area of the detector. The electrical filtering is necessary to sort them out so that a clean measurement may be made.

If you view the gratings from the front, the reference source is focused at say 12 o'clock on  $G_x$  and 3 o'clock on  $G_y$ . This gives the shear in the right direction. The shear is varied by moving  $G_x$  left and right and  $G_y$  up and down so that the spatial frequency of the square wave diffraction pattern decreases or increases. This has the effect of varying the gain in the feedback control system, and helps compensate for various target and atmosphere conditions.

#### 5.4.2 Wavelength Dependence

Now that we understand schematically how it works, let us consider the white light property. As Hardy<sup>1</sup> explains, the shear  $\theta_s$  between the overlapping images is defined by the equation

$$\sin \theta_s = \pm n \lambda v \quad n=1,3,5,\dots \quad (5.1)$$

where  $\lambda$  is the optical wavelength and  $v$  is the grating spatial frequency.

Denote the slope of the incoming wavefront  $\alpha(x)$ , and the focal length of lens L2  $F$ . The shear distance in the detector plane is given by  $S = \theta_s F$  and we have the following expression for the phase



difference between the sheared wavefronts in the detector plane:

$$\phi(x) = \alpha(x) \frac{S}{\lambda}. \quad (5.2)$$

The interference phase angle is the quantity of interest when the multiple images interfere. This angle is invariant to  $\lambda$  since  $S$  is proportional to  $\lambda$  for small angles. Hence  $\phi(x)$  is proportional to the wavefront slope, a dimensionless quantity, and the system operates in white light.

### 5.4.3 Electronics

Each detector outputs an ac signal in the kHz region whose phase is proportional to wavefront tilt in the corresponding subaperture. We have already mentioned that the extraneous sidebands are filtered out at this point. The remaining processing is amplification and AGC followed by phase detection with a phase-locked-loop. X and Y phase references are generated from the rotating gratings for use in this process.

For further details on this device, consult the references. Note that while some interferometers measure path lengths directly, this one measures wavefront slope instead. That is no major problem, but it certainly influences the processor, discussed next.

## 5.5 PROCESSOR

The detector array in a compensated imaging system typically is a square grid inside a circular aperture, as shown in Figure 5.3. The dots represent the MPM actuators; the actual physical locations in the image of the x and y tilt measurements are between the MPM actuators about where the  $\Delta$ s are in the figure. We have x and y phase differences, so what we would like to do is perform a least-squares fit of the data to solve this overdetermined system of equations for the best actuator displacements.

Hudgin<sup>19</sup> addressed this issue, concluding that both analog and digital processors were feasible. When one reads his paper, one wonders why he traveled to Fourier space rather than just solving the normal equations directly. Herrmann<sup>20</sup> evidently had the same question, and he provided a more coherent analysis of the problem. He also corrected a couple of Hudgin's errors. Hunt<sup>21</sup> also gave a general treatment of the problem in an explosion of matrix equations.

Hudgin used certain approximations valid for large arrays in his derivation, so it is not guaranteed optimum for finite arrays. His solution for an unknown phase involves the average of its four nearest neighbors plus a weighted sum of the four connecting phase differences.

The analog realization consists of a resistive network and many operational amplifiers; this is the approach taken in the current compensated imaging systems. The digital approach involves adders only; divisions are performed by shifting.

The exact solution is a least squares matrix problem. We can define a constant connection matrix  $A$ , relating the phase difference vector  $\Delta$  to the phase vector  $\phi$  by  $A \Delta = \phi$ . This matrix  $A$  consists of mostly zeros with a 1 and a -1 in each row.

The solution to this least squares problem is well known; the inverse of the "sample covariance matrix"  $A'A$  is multiplied by  $A'\Delta$  in real time to obtain the appropriate phases (MPM actuator signals). Since  $A$  doesn't change  $[A'A]^{-1}$  need only be precomputed once.

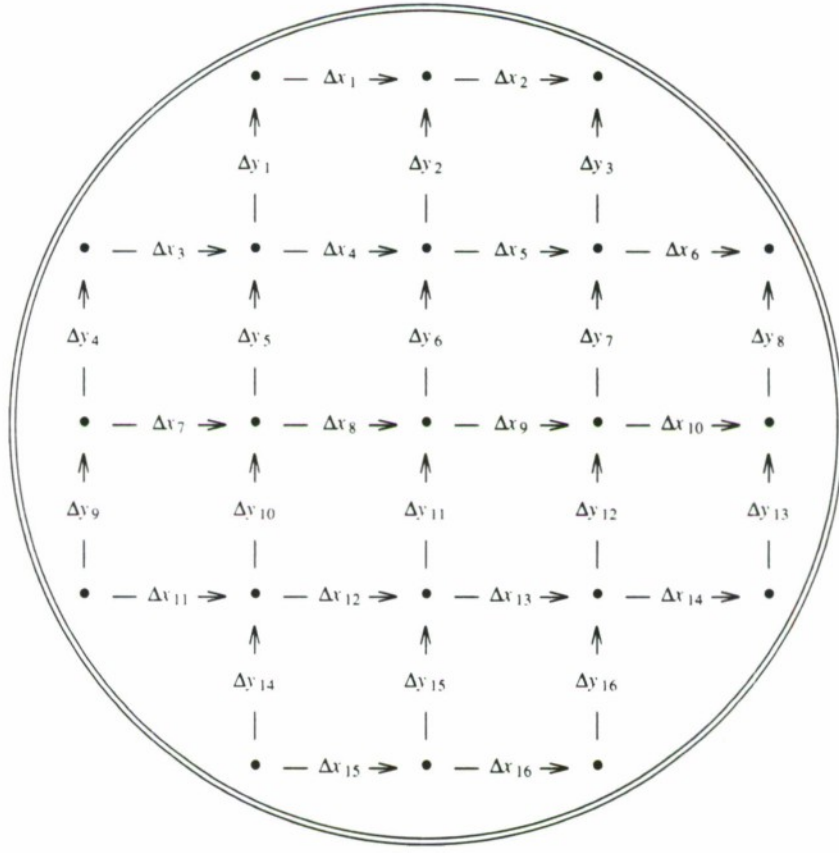


Figure 5.3. Wavefront reconstruction.

The analog version requires additional feedback loops to ensure that the tilt is entirely applied to the tilt equipment rather than using up the travel distance of the MPM. Similarly, the average deflection of the MPM is kept near zero, since absolute path distances are not important. These factors are more easily accommodated using digital techniques.

There are many issues which can be brought up such as noise propagation and time delay, but they would take us too far afield. Current designs mostly use analog processors, but it seems likely that future systems will employ digital processors, probably employing the optimum algorithm rather than Hudgin's approximations.

## 6. SPECKLE IMAGING

### 6.1 SPECKLE INTERFEROMETRY

#### 6.1.1 Labeyrie's Method

In 1970 Labeyrie<sup>3</sup> published a short paper in which he pointed out that the diffraction-limited power spectrum of the intensity of an astronomical object could be estimated using a sequence of short-exposure images. Fried<sup>9</sup> had already showed that short-exposure images had modulation transfer functions (MTFs) which were significant out to the diffraction limit. He did not, however, give any algorithm for converting a short term image or image sequence into a practical high-resolution image.

Labeyrie did not solve the high-resolution imaging problem either, but his insight was that rather than dealing with the standard incoherent quasi-monochromatic imaging equation Equation (3.32) one could instead profitably work with its magnitude squared

$$|I(u,v)|^2 = |O(u,v)|^2 |T(u,v)|^2. \quad (6.1)$$

Recall that  $T(u,v)$  is the transfer function of the atmosphere plus lens combination. Since there is a random phase added by turbulence, the mean value of averages of  $I(u,v)$  tends to zero for spatial frequencies beyond 1 cycle/arc sec or so. If one considers instead the magnitude squared of  $I(u,v)$ , the mean value remains significant.

##### 6.1.1.1 Frequency Domain Intuitive Explanation

Before discussing this more rigorously, consider the heuristic analysis of Roddier.<sup>22</sup> Recall our discussion of the interferometric view of imaging. An image can be imagined to be made up of the superposition of fringe patterns caused by pairwise combinations of points in the exit pupil. In the same way, we can imagine an aperture to be made up of subapertures larger than a point; the whole image can be considered to be a superposition of fringes from the pairwise combinations of subapertures.

As a point of departure, again consider the form of  $T(u,v)$  through a diffraction-limited lens. As we found in Section 3.6, defining  $\mathbf{f}$  to be our vector frequency  $(u,v)$ ,

$$T(\mathbf{f}) = \frac{N(\mathbf{f})}{N(0)} \quad (6.2)$$

where  $N(\mathbf{f})$  the *pupil redundancy* is the number of subaperture pairs which add to produce frequency  $\mathbf{f}$ . This is again proportional to the shaded area in Figure 3.5.

Now consider the situation of imaging through the atmosphere. Let our subaperture size be  $r_o$  and let the random phase delay  $\theta_k$  on subaperture  $k$  be constant and independent of the phase delay on the other subapertures. We can write our imaging equation as

$$I(\mathbf{f}) = O(\mathbf{f}) S(\mathbf{f}) \quad (6.3)$$

where the transfer function  $S(\mathbf{f})$  is given by the random sum

$$S(\mathbf{f}) = \frac{1}{N(0)} \sum_{k=1}^{N(\mathbf{f})} e^{i\phi_k}. \quad (6.4)$$



The sum is over all subaperture pairs contributing to frequency  $\mathbf{f}$  and the phase angle is the difference in phase between each such pair of subapertures.

The situation is mathematically a random walk. The average magnitude  $|S(\mathbf{f})|$  grows as the square root of the number of pairs. We conclude that the average power spectrum  $\langle |S(\mathbf{f})|^2 \rangle$  is proportional to  $N(\mathbf{f})$  rather than  $N^2(\mathbf{f})$ .

This analysis gives us helpful insight, but unfortunately in practice speckle imaging extracts these frequencies through the intermediate step of periodograms. The poor statistical properties of these estimators produce a large variance which worsens things. We will discuss this situation in more detail below.

#### 6.1.1.2 Spatial Domain Intuitive Explanation

There is also a very useful spatial domain heuristic analysis which we will discuss in this section. It originates in the classical astronomy problem<sup>23</sup> of identifying and analyzing binary stars. Assume we have an image of two objects separated by distance  $d$  such as depicted in Figure 6.1a. The point spread function of typical turbulence tends to produce multiple copies of the object being viewed at random positions within the fuzzy disk (Airy disk) corresponding to the long-term exposure. This is shown in Figure 6.1b. This effect is quite evident if bright stars are photographed properly with a large instrument and a short exposure.

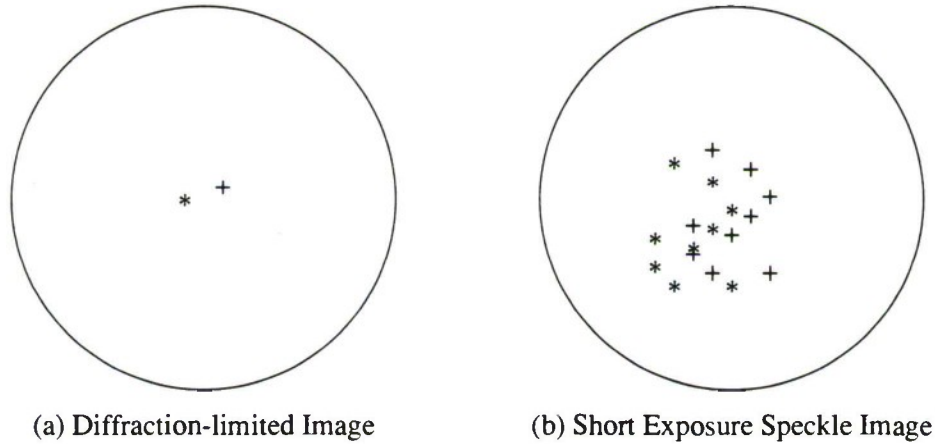


*Figure 6.1. Schematic speckle imaging.*

Now rather than consider the effect of the turbulence in the frequency domain, in terms of MTFs and periodograms, consider the equivalent autocorrelation function. The (ideal) autocorrelation function of the image in Figure 6.1a consists of the superposition of the autocorrelation functions of the two isolated objects at the origin and two cross-correlation terms at shifts of  $d$ .

Now consider the autocorrelation function of Figure 6.1b. It is obvious that for small shifts on the order of the diameter of the individual objects we will get a pretty good estimate of the ideal autocorrelation. The only errors will occur when the multiple images are spaced less than one of their diameters apart. Similarly, the autocorrelation for shifts of  $d$  will be quite accurate.



The main errors occur for other shifts when spurious cross-correlation terms appear. Recalling that the positions of the images of Figure 6.1b are random, it is clear that averaging many of these autocorrelation functions will tend to reduce the amplitude of these spurious correlations. Hence we obtain the proper diffraction-limited autocorrelation function as Labeyrie proposed. This argument is of course more convincing for isolated small objects than extended objects.

### 6.1.1.3 Summary

Now let us summarize the steps needed in Labeyrie's method. Note that the original algorithm used optical processing due to the unavailability of suitable digital computers. We will accordingly update the method for modern equipment.

We first obtain a short exposure image of the object under study. We compute the two-dimensional discrete Fourier transform (DFT). We then take the square of this DFT as a single estimate of the image power spectrum. This estimator, called a periodogram, is known<sup>24</sup> to be a very poor one in terms of bias and variance. While it is possible to improve the estimator by certain smoothing processes, that is obviously not what we desire since high resolution is our goal. The practical solution is to average many periodograms, as Labeyrie proposed.

There is one final step in the method. Since the atmosphere/lens combination has modified the spatial frequencies by some MTF, to restore the object power spectrum (autocorrelation) it is necessary to make a correction, as discussed below. This will be a critical step in later imaging algorithms and in some cases the most difficult step to perform.

## 6.1.2 OTF Corrections

### 6.1.2.1 Theoretical Analysis

Now that we have a heuristic picture of the turbulence MTF, we will consider briefly the rigorous analysis. Recall that in 1966 Fried<sup>9</sup> analyzed both the long term and short term imaging MTFs. Mathematically, he evaluated  $\langle S(\mathbf{f}) \rangle$ . Four years later Labeyrie published his paper, and there was a need to evaluate  $\langle |S(\mathbf{f})|^2 \rangle$ ; this was done by Korff<sup>10</sup> in 1973.

This was a rather difficult calculation involving the fourth order statistics of the amplitude of  $S$ . While certain approximations were made, the results have been shown to agree quite well with experiment. We will not delve into the mathematics here, although it is not too hard to follow if you are familiar with Tatarski's book and Fried's paper. The bottom line is not even an equation, since Korff was unable to solve the problem analytically, but a graph reflecting the results of computer calculations.

Figure 6.2 reproduces Korff's results. We can see the substantial improvement in high spatial frequency response using Labeyrie's method. Notice particularly that for the large diameter case, which might correspond to a 4 m telescope, the Labeyrie transfer function seems likely to support at least an order of magnitude better resolution. The exact figure depends on signal-to-noise considerations and so will differ from object to object. Of course as the seeing varies, even with constant telescope diameter, different transfer function curves are appropriate.

In the case of small diameters, it appears from Figure 6.2 that a MTF correction might improve long-term exposure data as well. Goodman and Belsher<sup>25</sup> analyzed the situation and concluded that this was possible.

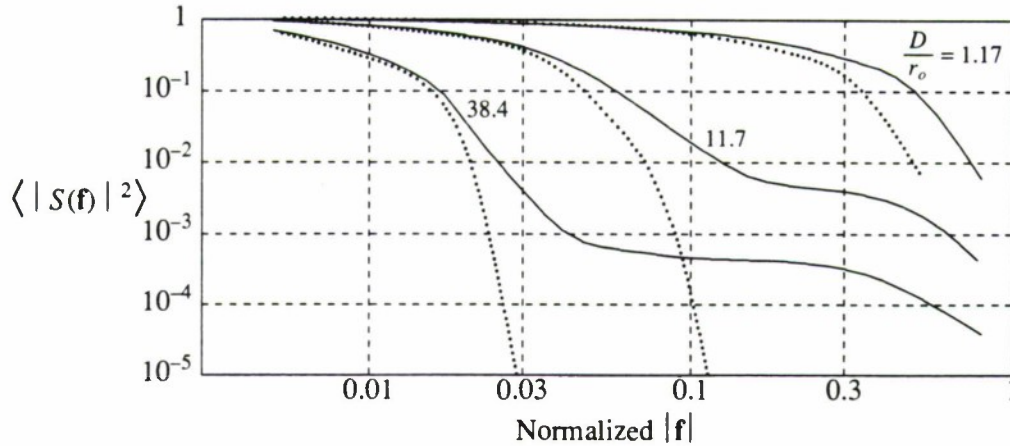


Figure 6.2. Turbulence MTF for Labeyrie (solid), long-term exposure (dotted).

### 6.1.2.2 Using Reference Stars

If there is one word which describes the theory of speckle imaging it is probably “approximation.” From the first principles of optics through the Van Cittert-Zernike theorem and the models of turbulence we have seen terms such as quasi-monochromatic, incoherent, plane wave, isoplanatic, Kolmogorov model, etc. Many of these approximations are quite good in the proper circumstances but there is a gradual erosion of confidence in the theory as they pile up one after the other. We still feel that our intuitive understanding is quite well served by these concepts, but it is logical to wonder how far a real system transfer function deviates from the theory.

There are also cases in which some of the required assumptions are not met, and we have no reason to believe that the theory is applicable. We might still have data available and want to restore its resolution as far as possible. What is needed is some metric which can guide us in our correction for the unknown MTF of the total imaging process.

This situation has been recognized from the beginning, and was even more important then since Korff’s paper and others had not yet been published. One solution, mentioned briefly by Labeyrie,<sup>3</sup> is to experimentally measure the long-term average of the short-term MTF of the atmosphere plus imaging system. This is conveniently done using an unresolvable star, since such a point object produces an image which is the point spread function (PSF) itself, i. e., the Fourier transform of the OTF. The phases of the OTF are not recoverable due to the turbulence, but the average magnitude gives us a useful MTF correction.

One problem occurs when the nearest suitable reference star is further than some isoplanatic angle from the object under study. Theory tells us that the PSFs will differ in this case. The solution lies in long-term averages. While a short sequence of degraded objects might experience a different MTF than the nearest reference star, we expect that a long-term average will differ much less. Experiment supports this argument.



There are still problems with reference stars. It is helpful if they are fairly bright, which limits their availability. If extremely bright objects such as low-orbit satellites are imaged, they may require a filter to avoid saturation which requires even brighter reference stars. One very interesting approach<sup>26</sup> is to create “artificial stars” using lasers. Although this is still in the preliminary investigation stage, there is an obvious attraction to producing “reference stars on demand.”

## 6.2 PHASE RETRIEVAL FOR SPECKLE IMAGING

Up to now we have discussed speckle interferometry, in which we cleverly process short-exposure images to obtain near-diffraction-limited autocorrelation functions. We do not, however, obtain actual images. As Labeyrie put it,<sup>3</sup> “Losing the phase makes it impossible to reconstruct the object, except if it has a center of symmetry.”

Fortunately, he was wrong in this assertion; there are methods by which the phase can be retrieved from the data. There are also purely mathematical methods in which the phases are retrieved from the magnitudes by the use of iterative procedures assuming certain constraints. We will discuss those algorithms next.

### 6.2.1 Knox-Thompson Method

The first practical phase retrieval method is due to Knox and Thompson.<sup>27</sup> This important paper showed that indeed phase information did exist in speckle data, and provided an algorithm to retrieve it. A one-dimensional simulation is the only result shown, although Knox<sup>28</sup> later provided two-dimensional simulation results.

Practically any algorithm can be analyzed in both the time (space) domain and the frequency domain. One is often clearer than the other, although which one sometimes depends on the observer. We have tried to present both approaches where possible in this report. Knox and Thompson explain their algorithm in the space domain by recourse to autocorrelation functions. It is clearer and fits in much better with our development to discuss it in the frequency domain.

Recall the imaging equation Equation (6.3), and the frequency domain intuitive explanation of incoherent imaging through the atmosphere. We can view our transfer function  $S(\mathbf{f})$  as being approximately made up of subapertures of dimension about  $r_o$  which have nearly constant phase shift. The shift is of course random over large distances.

When we compute the DFT of an image,  $i(x,y) \rightarrow I(u,v)$ , we obtain a two-dimensional array of spatial frequencies. While the absolute phases of these frequencies  $\phi(u,v)$  are the phases of the true image plus some random phases, if two phases  $\phi(u_1, v_1) \equiv \phi(\mathbf{f}_1)$  and  $\phi(u_2, v_2) \equiv \phi(\mathbf{f}_2)$  are closely spaced in frequency, the random phase components are nearly identical. Hence we can take the difference between such closely spaced phases and effectively obtain the difference between the true image phases. Closely spaced here means that the length of the frequency vector  $|\mathbf{f}_1 - \mathbf{f}_2| \equiv \Delta\mathbf{f}$  (in cycles/rad) is less than  $r_o/\lambda$ .

As the mathematicians would say, the problem is solved because we have reduced it to an equivalent problem already solved. That is of course the processor used in compensated imaging, and the calculation depicted in Figure 5.3. The situation is the same, with measured differences being combined to obtain the actual function. One distinction is that we have exactly the measurements shown in

Figure 5.3 in the compensated imaging case, while we can measure more differences in the Knox-Thompson (K-T) case if we want. This analogy is clear in light of history, but we can't be too hard on Knox and Thompson for not pointing it out. After all, compensated imaging did not exist at the time they did their work.

Now in practice the  $S(f)$  phase shifts are not perfectly uniform over a subaperture, no matter how small. Since we need multiple images to get the magnitudes with Labeyrie's method, we can obviously use those same images to compute multiple phase differences which can be averaged. The mean phase difference will be zero, so this process will reduce the variance. Since the phases are based on DFTs, we in fact need to average them to get reasonable estimates for the same reason Labeyrie's method needs multiple images.

A more serious problem occurs when the magnitudes of the spatial frequencies become small or zero. Then the phases are either undefined or highly variable, and our network of differences becomes corrupted or has a hole rather than being continuous. This is really the theoretical Achilles heel of the K-T method, and prevents it from standing alone as a completely general phase retrieval scheme. A recent paper<sup>29</sup> attempts to overcome this problem.

We should say a word about the computations associated with K-T. If we measure the phase differences say across every row of our array and just one column (or vice versa), we have a unique solution for the phases which can easily be computed. This was the original approach of K-T. A rather obvious improvement was to do it twice, once relying primarily on row differences, and once relying on column differences, and then averaging the results.

In light of our discussion of the compensated imaging processing, we would prefer to solve a least-squares problem using all of the differences simultaneously. Recall that the dimension of the matrix problem matches the number of subapertures in the compensated imaging case. In the K-T case, we probably have 10 to 100 spatial frequencies in each subaperture, so rather than having a least-squares problem of dimension say 100, we have one with dimension 1000 to 10000 or more. This is not cause for panic, especially since we do not need to calculate in real time, but it will require more processing.

Using the least-squares approach we could include diagonal differences as well, perhaps obtaining a more accurate result. Since the spatial frequency spacing is greater on the diagonals by  $\sqrt{2}$ , we might assign those errors less weight. If diagonals are included, the sparse matrix being solved becomes less sparse. This is not a problem, however, because just as in the compensated imaging case we would pre-invert the constant matrix  $A^T A$  once.

### 6.2.2 Triple Correlation Method

If we let the vector frequencies  $(u, v) \equiv \mathbf{f}_i$  and similarly the vector spatial coordinates  $(x, y) \equiv \mathbf{x}_i$ , we can define the triple correlation of an image by

$$i^{(3)}(\mathbf{x}_1, \mathbf{x}_2) = \int_{-\infty}^{\infty} i(\mathbf{x}) i(\mathbf{x} + \mathbf{x}_1) i(\mathbf{x} + \mathbf{x}_2) d\mathbf{x}. \quad (6.5)$$

The Fourier transform of the triple correlation is known as the bispectrum

$$I^{(3)}(\mathbf{f}_1, \mathbf{f}_2) = I(\mathbf{f}_1) I(\mathbf{f}_2) I(-\mathbf{f}_1 - \mathbf{f}_2). \quad (6.6)$$



The average bispectrum of the image can be related to the bispectrum of the object through the average bispectrum transfer function  $S^{(3)}$

$$\langle I^{(3)}(\mathbf{f}_1, \mathbf{f}_2) \rangle = O^{(3)}(\mathbf{f}_1, \mathbf{f}_2) \langle S^{(3)}(\mathbf{f}_1, \mathbf{f}_2) \rangle. \quad (6.7)$$

In our discussion of the K-T method we have alluded to the distinction between frequency and space domain explanations of algorithms. Things get much worse when one contemplates explaining the triple correlation equations above. We have the usual time/space dichotomy, but in addition we can group the terms different ways to produce different models.

If we group two of the terms of Equation (6.5) we can consider them to produce an autocorrelation function which is masked by the third term.<sup>30,31</sup> With certain types of objects this can produce a useful conceptual model. Weigelt<sup>32</sup> adopted this *speckle masking* approach when he first proposed the method.

If we consider the three terms of Equation (6.6) on an equal basis, we can employ the *phase closure* paradigm<sup>22</sup> which originated in radio astronomy. The basic idea is to add three phase terms (multiply three complex numbers) which have common errors with alternating signs so that the errors cancel out. Manipulations of the resulting composite *closure phases* are able to extract the phases of interest.

Naive application of triple correlation can require prohibitive computation and storage, so heuristic modifications of the algorithm have been common with a corresponding lack of rigor. Freeman *et al*<sup>33</sup> have written an interesting paper comparing various triple correlation algorithms to Knox-Thompson with a more appealing theoretical basis. They also take a frequency domain approach vaguely similar to our Knox-Thompson discussion.

We have defined the triple correlation and bispectrum as mathematical objects without relating them to our problem of phase retrieval. That is accomplished with the aid of the fact<sup>30</sup> that  $S^{(3)}$  is real. It follows from Equation (6.7) that the image triple correlation has the same phase as the object triple correlation.

We will call the phase of the bispectrum  $\beta$  and the phase of the object  $\phi$ . From Equation (6.6) we obtain the recursive relationship

$$\phi(\mathbf{f}_1 + \mathbf{f}_2) = \phi(\mathbf{f}_1) + \phi(\mathbf{f}_2) - \beta(\mathbf{f}_1, \mathbf{f}_2). \quad (6.8)$$

This expression says that given the phases at frequencies  $\mathbf{f}_1$  and  $\mathbf{f}_2$  and the bispectrum  $\beta(\mathbf{f}_1, \mathbf{f}_2)$ , we can compute the phase at frequency  $\mathbf{f}_1 + \mathbf{f}_2$ . Recursively we can compute all of the phases. To start the recursion we require a couple of image phases. We can arbitrarily set these since they relate to the position<sup>30</sup> of the object.

A key feature of triple correlation is the multiplicity of estimates of each phase which are available. We can decompose the frequency  $\mathbf{f}$  into many different sums  $\mathbf{f}_i + \mathbf{f}_j$ , each of which yields a different estimate. While these can be combined in obvious ways such as averaging, just as in the K-T case it is more profitable to solve a least-squares problem. The *minimum-variance weighting* discussed by Freeman *et al*<sup>33</sup> is perhaps the best estimator to date.

It can be easily shown that the four-dimensional triple correlation function contains the K-T information in certain planes. Triple correlation should always do as well or better than K-T since a valid estimator could just use the K-T data and duplicate the K-T algorithm. By definition, a minimum-variance estimator which does not use K-T must be doing as well or better than K-T.

The triple correlation algorithms' biggest problem is their required storage and processing. If we have digital images of dimension 256 by 256, and we store the entire triple correlation function in single precision 4 byte floating point, storage of 17 Gbytes is required, larger than the largest magnetic disks! The processing required to compute such a function is also prohibitive.

Some of the algorithms which estimate phase from the bispectrum are not too computationally demanding, but the minimum-variance method mentioned above requires solution of matrices of possibly excessively large dimension. The demonstration of the method on one-dimensional data does not give any confidence that two-dimensional application is feasible.

This is certainly an area of active research. It is known<sup>33,34</sup> that there are extensive symmetries in the triple correlation. For example, in the one-dimensional case (two-dimensional triple correlation) we can work with one region in the first quadrant which comprises about 1/16th of the total function. As the theory progresses, it is hoped that the most important regions of the triple correlation function can be identified and used effectively. The cited papers make some progress in this direction.

### 6.2.3 Phase Reconstruction from Magnitude

It has been known for years that the problem of reconstructing the phase of a one-dimensional sequence from its magnitude is intractable; there are hopelessly many solutions. Until about 1978 everyone assumed that the situation would be no better in the two-dimensional case. The theoreticians did not discover the error in this assumption until practical algorithms for phase retrieval were published.

In 1972 Gerchberg and Saxton<sup>35</sup> published an important paper describing an iterative algorithm for phase retrieval. Their application had available magnitude information for both a two-dimensional function and its Fourier transform. For example, electron microscopy and X-ray crystallography can satisfy this requirement by obtaining intensities in both the image and diffraction planes.

The algorithm proceeds as shown in Figure 6.3. Initial random phases are generated, uniform on the interval  $(-\pi, \pi)$ . They are combined with the known image magnitudes and the result is Fourier transformed. The phases of the FT are likewise combined with the known FT magnitudes and the result is transformed back. Again the phases are combined with the known image magnitudes and one iteration has been completed.

While interesting, there is no direct application of this algorithm to phase retrieval for speckle imaging. It led, however, to the important discovery by Fienup<sup>36,37,38</sup> of an iterative algorithm suitable for speckle imaging. Fienup's insight was that one could generalize the Gerchberg-Saxton algorithm so that rather than simply combining the FFT phases with the measured magnitudes, one applied some other constraint. Since we have the FT magnitudes in speckle imaging, that part of the algorithm can proceed in the same way. In the image domain, suitable constraints suggested by Fienup include *finite support*, in which the image is assumed to be zero outside some region, and non-negativity, since intensities cannot be negative. Figure 6.4 shows Fienup's algorithm.

Fienup supplied examples, including blind tests, as well as algorithm modifications which enhance convergence. There are certain ways the algorithm can stagnate, and artifacts which may occur in these cases. Fienup has given fixes<sup>38</sup> for many of these problems. These make interesting reading but they are a little beyond the scope of this report.

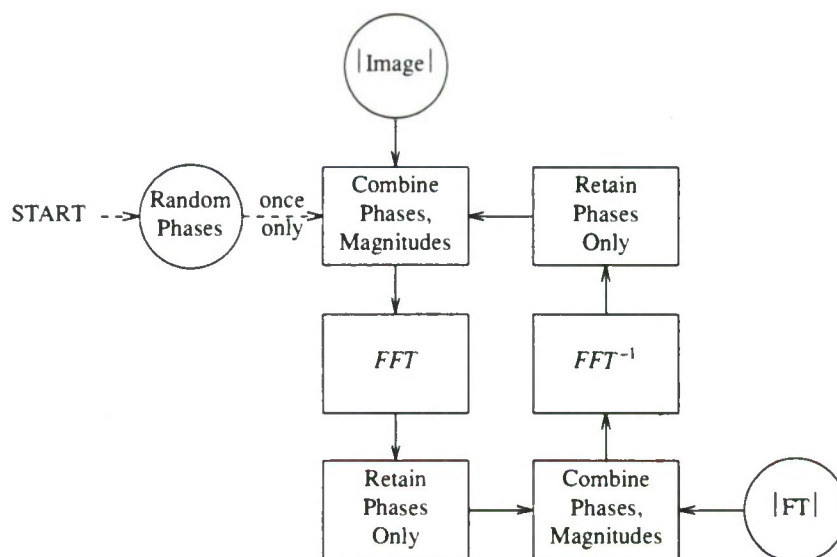


Figure 6.3. Gerchberg-Saxton algorithm.

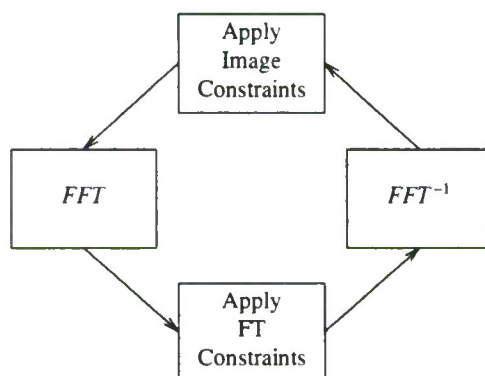


Figure 6.4. Fienup's algorithm.

Once Fienup had published his work, theorists went scurrying off to try to explain why it worked. The first outstanding issue concerned the uniqueness or non-uniqueness of the solutions. An algebraic explanation was finally produced involving polynomial factoring. While any polynomial in one variable can be factored, very few polynomials in two variables have this property. Hence most images have unique phase solutions. Hayes<sup>39</sup> has provided a lucid summary of the mathematics of phase reconstruction.



Once this mathematical foundation was laid, attention turned to better methods of phase retrieval. It has been found that while systems of equations can be written whose solution is the desired phase, their solution is computationally impractical in all but the smallest problems.

The next obvious area of mathematical investigation is iterative algorithms such as Fienup's algorithm. Perhaps a more general mathematical understanding of such algorithms would lead to better algorithms. One mathematical framework<sup>40</sup> describes these algorithms in terms of projections of convex sets (POCS) in Hilbert space. An interesting recent paper<sup>41</sup> claims to generalize things further by appealing to some results of nonlinear programming. To make a long story short, nothing has yet emerged to challenge Fienup's algorithm in the speckle imaging application. We do understand it a lot better, however.

## 6.3 SPECKLE PARAMETERS

### 6.3.1 Signal-to-Noise Ratio

Speckle imaging has been developed and used by astronomers, so issues of most concern to them have received the most attention. In astronomy, most of the objects of greatest interest are extremely faint; bright objects are a lower priority. Faint objects also represent a greater technical challenge.

In space surveillance, on the other hand, in order to obtain usable resolution on man-made objects using telescope apertures on the order of a couple of meters, we consider mainly objects in relatively low orbits. For example, to achieve 50 cm resolution with a 2 m telescope we would confine our observations to objects lower than 2000 km. In this regime, with solar illumination, the satellites are quite bright objects.

It turns out that the behavior of the signal-to-noise ratio (S/N) is different for the two cases. Dainty<sup>42</sup> gives a space-domain calculation for the case of a faint double star. He computes the variance of the peak correlation, which occurs at the binary star spacing. The main features of his findings are as follows:

- (a) The rms S/N is proportional to the number of detected photons per picture.
- (b) The S/N is proportional to the telescope diameter.
- (c) The S/N is inversely proportional to the diameter of the long-exposure image, or directly proportional to the seeing.
- (d) The S/N is inversely proportional to the number of resolution cells in an extended object.

Photon noise produces a bias in the spectral estimates which can be removed. Goodman and Belsher<sup>25</sup> present a clear analysis of the problem based on Poisson statistics. It was later shown<sup>43</sup> that if a photon-counting camera is available, better performance is obtained by making this correction using the actual number of photons in the image rather than the average number. Dainty and Greenaway<sup>43</sup> also discuss noise reduction by elimination of frames containing less than two photons. Nisenson and Papaliolios<sup>44</sup> extended the analysis from simple speckle interferometry to Knox-Thompson processing. Ayers *et al* recently published an even more comprehensive paper<sup>45</sup> including an analysis of triple correlation.



Miller<sup>46</sup> gives an exhaustive analysis of many noise sources. His assumptions are more general than Dainty's, and his conclusions are somewhat different numerically. It is important to check carefully just what is being assumed in noise analyses; there are differences in light levels, detector characteristics, and the quantity whose statistics are being specified.

Let us consider more carefully the case of bright objects. We have already remarked above that periodograms are rather poor estimators. In fact, under reasonable (Gaussian) assumptions it can be shown<sup>24</sup> that the standard deviation of periodogram estimators is about equal to the mean. This is true no matter how long a data record is Fourier transformed. The explanation lies in the fact that while longer periodograms involve more input data, we are also estimating proportionately more parameters.

It follows from this that the power spectrum estimate of Labeyrie's method has S/N of approximately unity for bright objects. Note that here we neglect detector noise along with a few other possible noise sources. These do not change things appreciably in many cases of imaging bright objects with high quality equipment. Hence unity is the maximum value the S/N can assume in this type of processing.

The S/N is increased by averaging multiple images. If periodograms of  $n$  independent images are averaged, the S/N will increase by a factor of  $\sqrt{n}$ . This can be understood in many ways; for example, the "signal" is being integrated coherently and its power is increasing as  $n^2$ , while the "noise" is integrated non-coherently so its power increases as  $n$ . The periodogram S/N thus increases as  $n$ , but we take a square root to obtain the estimate of the spatial frequency magnitude so its S/N increases as  $\sqrt{n}$ .

If we are interested in a S/N of 20, some 400 independent periodograms must be averaged, *regardless of the brightness of the object*! Of course, in the photon-limited region the individual S/Ns are lower, and sometimes many thousands of periodograms are required.

This brief summary tried to convey the idea that accurate S/N analyses for general cases are rather complicated. The understanding we have achieved here will suffice for our purposes. A careful analysis of S/N for each real experiment is recommended.

### 6.3.2 Integration Time

So far we have considered our images as "instantaneous" snapshots through some turbulent atmosphere; in reality, our detector must integrate for some finite time. Expressing this time dependence Equation (6.3) becomes

$$I(\mathbf{f}, t) = O(\mathbf{f}) S(\mathbf{f}, t). \quad (6.9)$$

When our detector integrates over a time  $\Delta t$ , the detected image is not the  $I(\mathbf{f})$  of Equation (6.3) but rather  $\hat{I}(\mathbf{f})$  where

$$\hat{I}(\mathbf{f}) \equiv \int_0^{\Delta t} I(\mathbf{f}, t) dt. \quad (6.10)$$

When we do speckle processing, we have (ignoring scaling factors)

$$\langle |\hat{I}(\mathbf{f})|^2 \rangle = |O(\mathbf{f})|^2 \langle \left| \int_0^{\Delta t} S(\mathbf{f}, t) dt \right|^2 \rangle. \quad (6.11)$$

We are interested in the last term, the average squared magnitude of the integrated optical transfer function, for various values of  $\Delta t$ . Recall that Korff<sup>10</sup> studied this term for long and short exposures.

Roddier and Roddier<sup>47</sup> generalized his results to the intermediate case using the so-called “Taylor hypothesis.” When speckle patterns evolve with time, their behavior is usually considered to involve a combination of speckle motion and “speckle boiling,” in which the individual speckles fluctuate. In the Taylor hypothesis the atmosphere is treated as a fixed snapshot of turbulence which the wind is blowing in some direction at some speed. This assumption is sometimes questionable, but it did produce useful results in agreement with some experimental data.

If we consider the effect of exposure time on the MTF, long exposures result in a greatly attenuated high-frequency wing of the MTF, while instantaneous exposures contain useful high-frequency MTF information out to the diffraction limit, as Korff showed theoretically. In the case of intermediate exposure times, the MTF not surprisingly takes intermediate values.

Unfortunately, Roddier and Roddier required fourth-order moments for their calculations, and the mathematics is too complicated to reproduce here. We will content ourselves with a few remarks on their results.

For a 5 m telescope,  $r_o$  of 13 cm, and 10 m/s wind velocity, exposure times up to 20 ms had only negligible effect on the MTF. Smaller telescopes were more affected by exposure time; under the same conditions a 1.5 m telescope suffered negligible depression of the MTF for exposures up to 10 ms.

High frequency components of the MTF were more affected by exposure time than low frequency components. This would be expected if we remember our model of individual speckles moving around the image. Each MTF frequency component can be considered to be obtained by multiplying a spatial frequency basis function by the image and summing. A small motion affects the high frequencies more than the low frequencies since it involves motion of a greater fraction of a spatial frequency wavelength prior to the correlation operation.

In 1978 Karo and Schneiderman<sup>48</sup> published a more comprehensive and more accessible, although perhaps less original, paper on exposure times and bandwidths. They discuss the simulation of exposure time by superimposing multiple independent images. They report measurements of the effect of exposure time using the 1.6 m telescope at the AMOS facility in Hawaii. Exposures of 5 ms were the shortest they used, but indications were that shorter exposures might produce even better results. When the exposure reached 40 ms, the MTF dropped into the noise at about 85 percent of the diffraction limit. Some MTF above the seeing limit was observed even at 320 ms.

As long as the MTF stays sufficiently above the noise, correction for excessive exposure time is theoretically possible. Of course the overall MTF correction error will increase as we attempt to make ever more heroic compensations. This will adversely affect the rest of our speckle imaging algorithms in some way. Hence it is important to be aware of the S/N when correcting for exposure time effects.

If one has substantially more light per exposure than needed to keep the single-frame S/N near unity, it clearly makes sense to shorten the exposure time. Shortening the time by a factor  $n$  will increase the total S/N by a factor of  $\sqrt{n}$  as long as the individual frames retain a S/N near unity.

On the other hand, if the object is very dim it can be shown that the single-frame S/N is proportional to the number of photons. Hence it pays to integrate longer and combine fewer frames. Clearly there is an optimum integration time which is discussed by O'Donnell and Dainty.<sup>49</sup>



### 6.3.3 Bandwidth

Another important issue is the effect of optical bandwidth on MTF. As Roddier<sup>50</sup> points out, there are three effects of optical bandwidth which tend to reduce the MTF for high spatial frequencies. Some recent detailed theoretical references<sup>51,52</sup> are not the most readable papers imaginable. Accounts of good experimental work<sup>48</sup> are recommended to obtain an intuitive grasp of bandwidth effects.

Perhaps the most basic effect of excessive bandwidth is a loss of temporal coherence over the telescope aperture. Since the paths through the turbulence have varying lengths, causing the phase shift which is our main difficulty, there is a corresponding time delay for different parts of the aperture. In order to apply the basis of speckle imaging, the Van Cittert-Zernike theorem, we need the quasi-monochromatic condition. We are pushing the definition of quasi-monochromatic in practice, but we certainly require some level of temporal coherence. Clearly excessive bandwidth can completely destroy coherence.

Karo and Schneiderman<sup>53</sup> discuss this condition, arriving at the conclusion that for best results one should use  $\Delta\lambda/\bar{\lambda}$  of 0.1 to 0.05. They give a physical discussion using the analogy of a good quality conventional lens.

However this should depend on the telescope diameter as well as the seeing. It is easy to see that the coherence length of a uniform spectrum over the bandwidth  $\Delta\lambda$  is roughly  $\bar{\lambda}/\Delta\lambda$  wavelengths or  $\bar{\lambda}^2/\Delta\lambda$ . (For example, if the bandwidth fraction is 1/10, the frequency extremes will be completely out of phase after about 10 wavelengths.) The total path length difference (phase shift) over the telescope aperture should not exceed this quantity; the problem is to determine that phase shift.

Assume that a telescope of diameter  $r_o$  can handle essentially  $\Delta\lambda/\bar{\lambda}$  of 60 percent (entire visible spectrum); the wavelength extremes are just reaching the point of non-coherence. If we increase the telescope diameter to  $D > r_o$ , we need to maintain coherence over the frequency extremes across the larger diameter  $D$ . We can do this by reducing the bandwidth proportionately, arriving at the often-quoted rule

$$\frac{\Delta\lambda}{\bar{\lambda}} < \frac{r_o}{D}. \quad (6.12)$$

The second bandwidth effect is the dispersion introduced by the atmosphere if the telescope is not pointing directly at the zenith. This can be corrected by a prism arrangement and so represents less of a fundamental limitation than the other effects.

The third effect is a wavelength-dependent magnification of the entire image. As discussed by Roddier,<sup>50</sup> this leads to a requirement similar to Equation (6.12).

The situation is quite similar to the exposure time case. It is necessary to push the bandwidth as high as possible to enhance S/N ratio. When this is done, the higher portion of the MTF is depressed. Again, it is theoretically possible to correct for excessive bandwidth subject to ultimate S/N limitations. Just as in the exposure time case, the theory involves enough approximations to keep one alert to the possibility that experimental conditions may cause unexpected behavior. Any available experimental measurements of bandwidth effects during data collection, or with the equipment used for data collection, are probably worth examining.

### 6.3.4 Field of View

The field of view over which speckle imaging or adaptive optics works is often loosely defined to be the “isoplanatic patch” which variously is described as 1” to 5” or even more. Fried wrote an often referenced paper<sup>54</sup> providing theoretical analysis of five different types of isoplanicity, one of which was speckle interferometry isoplanicity. The differences essentially involve the equipment used and the exposure times. The goal was to characterize isoplanicity in each case so that corrections could be made for its effects. Another important theoretical paper<sup>55</sup> by Korff *et al.* gives a deeper theoretical analysis of isoplanicity applicable for the speckle imaging case. This is not the easiest paper in the world to read.

It is again more helpful for our purposes to look at some experimental work. Schneiderman and Karo discussed the results of some measurements at AMOS in 1976 in a paper<sup>56</sup> on binary star speckle interferometry. Unfortunately, they specialized their analysis to the problem of resolving two (individually) unresolvable stars. The resulting parametric approach is based on fringe visibility and is not directly applicable to extended objects. They also had some experimental difficulties which cast some doubt on their experimental results. The importance of their paper is that it used the technique of computing the cross-correlation between two speckle images formed from double stars of known separation. Another similar paper<sup>57</sup> on measures of isoplanicity using binary star systems was published at about the same time.

The cross-correlation gives us a measure of the nonisoplanatic effect. If we take out the average separation of the two images  $a$  and  $b$ , and let the coordinate system of each image be centered, the simple cross-correlation mentioned above becomes one point of the cross-correlation function  $R_{ab}(0)$ . If we consider the more general correlation function  $R_{ab}(x)$  where  $x$  is the magnitude of vector correlation distance, we study its Fourier transform the cross-spectrum  $S_{ab}(u)$ . The integral of  $S_{ab}$  is  $R_{ab}(0)$ . Korff *et al.*<sup>55</sup> showed the important role of the cross-spectrum as a measure of the effect of nonisoplanicity on speckle imaging. As might be expected, the higher spatial frequencies are attenuated more in the cross-spectrum.

Ebersberger and Weigelt published an interesting study<sup>58</sup> in which they computed correlation functions and cross-spectra of speckle images of binary stars with various separations. The correlation ranged from 55 percent for separations of 2.9” down to 8 percent for 7.8” separations. In addition they showed cross-spectra of binary stars.

For 2.9” separation, the cross-spectrum dropped to 0.5 at a normalized spatial frequency  $u$  of about 0.6; it dropped to zero at about 0.9. For the 4.3” separation the drop to 0.5 occurred at frequency 0.35, with zero again reached at 0.9. For the 7.8” separation the numbers were about 0.1 and 0.8.

Christou and Hege<sup>59</sup> continued in this vein, showing additional plots of normalized cross-spectrum. They identified this function as the correction factor required in speckle holography.

We have not discussed this technique, but briefly if a point source is near the object being imaged, the phase of the object may be retrieved directly. From an autocorrelation point of view<sup>60</sup> if the point source is at a distance of more than twice the diameter of the object, the autocorrelation function of the image will consist of three parts. The part near the origin may be discarded and the cross-terms will be images of the object. This technique also can be explained<sup>61</sup> by analogy to holography.



Returning to our discussion of isoplanicity, since the reference object in speckle holography has some angular separation from the object being imaged, we have a need for a correction. Dividing by the normalized cross-spectrum effects this correction.

We can interpret drops in the cross-spectrum as reductions in  $S/N$ . Hence we lose the most  $S/N$  at the high spectral frequencies. In speckle imaging, if we have enough data of good  $S/N$ , we can overcome this problem by statistical averaging. If we don't, we will lose some resolution. Things seem worse for adaptive optics. The instantaneous estimate of the turbulence phase shift will be noisier, so our real-time correction will be poorer, especially at the high spatial frequencies.

In conclusion, isoplanicity is an elusive concept which must be considered in the context of the actual system under study rather than as an absolute quantity dependent only on the atmosphere. It seems inescapable that its effects will be observed whenever the field of view of an image exceeds one or two arc seconds. It may represent a substantial problem for satellite imaging due to the large angular extent of many low-earth-orbit satellites.

## 7. APPLICATION TO SPACE SURVEILLANCE

### 7.1 INTRODUCTION

We have completed our review of the new adaptive and speckle techniques for high-resolution optical imaging. By this time, the reader should be able to follow the gist of the literature on these subjects. To that end, we have used much of the terminology and notation which is current with researchers in these areas.

We wish to consider the new techniques together in this section, taking a more unifying viewpoint. The adaptive system will be analyzed as a coherent integration prior to the noncoherent speckle processing.

We will also discuss the peculiar problems of imaging satellites rather than the astronomical objects which dominate the unclassified literature. We will consider the limits on integration time imposed by satellite motion. The bistatic nature of incoherent optical imaging will be contrasted with typically monostatic alternatives such as radar imaging.

Adaptive systems will always contain small errors. Since we are adaptively correcting phase, these errors will manifest themselves in this domain. Atmospheric scintillation will also produce small errors which are unaffected by adaptive phase corrections. We will explain the similar effects of small amplitude and phase errors on the OTF by appealing to well-known results of communications theory.

To make the transition from speckle interferometry to speckle imaging we need to select a phase-retrieval algorithm. We will provide guidelines for that selection decision which depend on the data; our satellite imaging application will then dictate the decision.

We have discussed the various errors and degradations which can hinder the new imaging techniques at some length. While it is obviously preferable to avoid these errors and degradations as much as possible during experiment design and data collection, there are times when unknown degradations have affected our data. Most astronomical data collections may be repeated at our leisure (excepting the occasional supernova) subject only to equipment availability. This is not the case in satellite surveillance, since satellite lifetimes are comparatively short and the most interesting data may involve short, unique events.

In cases where a data set is irreplaceable, it is desirable to develop techniques of evaluating its quality as well as its potential for enhancement using speckle techniques. The interferometer signals used in adaptive optics are one clear source of data quality measurement, but they do not exist in the speckle case and may not always be recorded in adaptive systems due to the volume of data. We will describe some measures of data quality which are calculated from short-term images themselves.

### 7.2 GENERALIZED OPTICAL SURVEILLANCE

#### 7.2.1 Block Diagram

For purposes of discussion, consider the generalized system depicted in Figure 7.1. The dashed boxes may or may not exist in a given system. This may be thought of either as the combination of adaptive optics and optional speckle post-processing, or speckle imaging with optional adaptive

pre-processor. The object being imaged is a satellite. We allow the possibility of using a reference object to assist either the adaptive optics or the speckle processing. This might be either a natural reference object such as a star or artificial stars created by a laser<sup>26</sup> in the atmosphere.

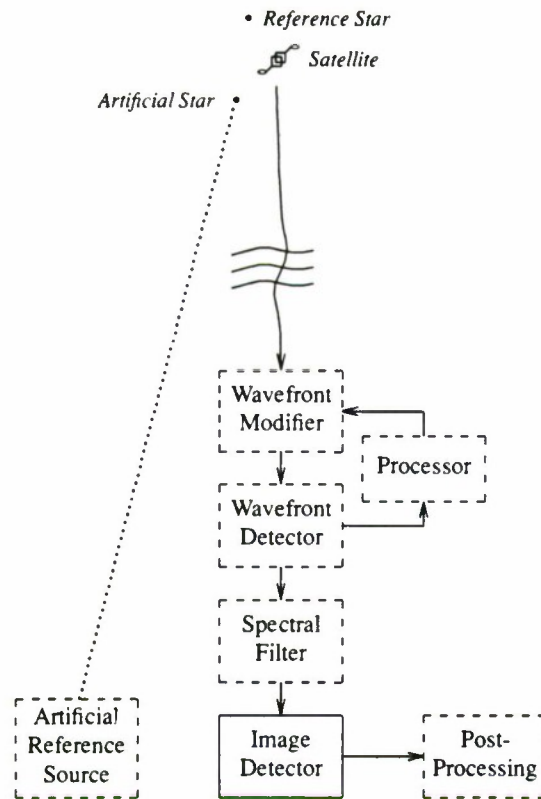


Figure 7.1. Generalized optical surveillance system.

There are two physical effects that we are estimating no matter how we operate this system. One is some measure of turbulence, either on a short-term or long-term basis or both. The other is of course an estimate or sequence of estimates of the spatial frequencies of the target itself. The former is used to correct the latter.

### 7.2.2 Effect of the Wavefront Modifier

Light from the satellite being imaged passes through the turbulent atmosphere and enters the optional wavefront modifier. This device can be considered to be a time-varying matched filter. It provides coherent integration gain by matching the effect of the turbulence.

Recall from communications theory that when a signal with some specified frequency distribution is received in the presence of white noise, a matched filter maximizes the output S/N. The matched filter has frequency spectrum which is the complex conjugate of the signal spectrum, or equivalently impulse response which is the time-reversed signal itself.



There are some differences in the physics of our situation but very little difference in the mathematics. Rather than time functions we are concerned with space functions. The finite waveform duration  $T$  of matched filter derivations is replaced by the telescope aperture  $D$ . We also are working in two spatial dimensions rather than one time dimension; the two-dimensional analysis is a straightforward extension of the one-dimensional.

Since we are performing our wavefront correction in the pupil plane, we are dealing with the mutual coherence function so it makes sense to think of the frequency-domain interpretation of the matched filter. The atmosphere is being modeled as a filter with unity magnitude at each spatial frequency and some phase shift. Each subaperture corrects for the atmospheric phase shift by producing a conjugate phase shift, the definition of the matched filter.

What remains is to quantify the coherent integration gain that we obtain from a perfect wavefront matched filter. Recall the frequency domain heuristic explanation of speckle imaging discussed previously in Section 6.1.1.1. Based on the interferometric view of imaging, we can imagine the transfer function of the atmosphere to be composed of a two-dimensional array of subapertures whose phase shift is constant and independent of the other subapertures. We can use this model both to compute the transfer function  $S(\mathbf{f})$  as before and to derive the S/N advantage of the matched filter.

We previously showed that the speckle transfer function grows as the pupil redundancy  $N(\mathbf{f})$  rather than as  $N^2(\mathbf{f})$  due to the noncoherent nature of Labeyrie interferometry. This implies that the spatial frequency MTF is proportional to  $\sqrt{N}(\mathbf{f})$ .

Unfortunately, we cannot directly achieve the theoretical S/N of the speckle process but must instead compute periodograms which have poor statistical properties, e. g., a standard deviation on the order of the mean. Hence we face a S/N limit at all spatial frequencies of unity. This could represent a tremendous loss in the case of very high light levels and fixed integration time. Practically we have finite light, and we are able to select our integration time if we use suitable equipment. The solution is to use very short integration intervals and many of them, so that the photon-limited S/N per frame is not much higher than unity to begin with.

In the case of a matched filter wavefront corrector, the MTF is just the magnitude of the perfect circular aperture transfer function which is proportional to  $N(\mathbf{f})$ .

Now that we understand qualitatively the effect of coherent and noncoherent integration on the MTF, we will turn our attention to the S/N improvement due to matched filtering. If we consider the image as a whole, we will obtain a coherent integration gain of  $D/r_o$  in each direction, or a total integration gain of  $(D/r_o)^2$  over a telescope of aperture  $r_o$ .

We are more interested, however, in the gain at individual spatial frequencies  $\mathbf{f}_k$ . Recall that for bright images the maximum S/N of a periodogram frequency is unity *for frequencies beyond the seeing limit*. The matched filter circumvents this limitation by coherently integrating spatial frequencies all the way to the diffraction limit. Hence the seeing limit becomes the diffraction limit and the S/N can exceed unity at all spatial frequencies. Of course the improvement at a given frequency  $\mathbf{f}$  will depend on  $N(\mathbf{f})$ .

Numerically we are motivated to find the transfer function  $T(\mathbf{f})$  of an ideal circular aperture which Equation (6.2) relates to  $N(\mathbf{f})$ . We have defined  $\mathbf{f} \equiv (u, v)$  but  $T(\mathbf{f})$  actually only depends on the magnitude of this vector frequency,  $\sqrt{u^2 + v^2}$ . We are interested in computing the ratio of the overlap area circles in Figure 3.5 to the area of one circle. A straightforward calculation provides us with the result that



$$T(g) = 1 - \frac{2}{\pi}(g\sqrt{1-g^2} + \sin^{-1}g) \quad (7.1)$$

where  $g$  is the ratio of the vector spatial frequency magnitude to the spatial frequency diffraction limit. This function is shown in Figure 7.2.

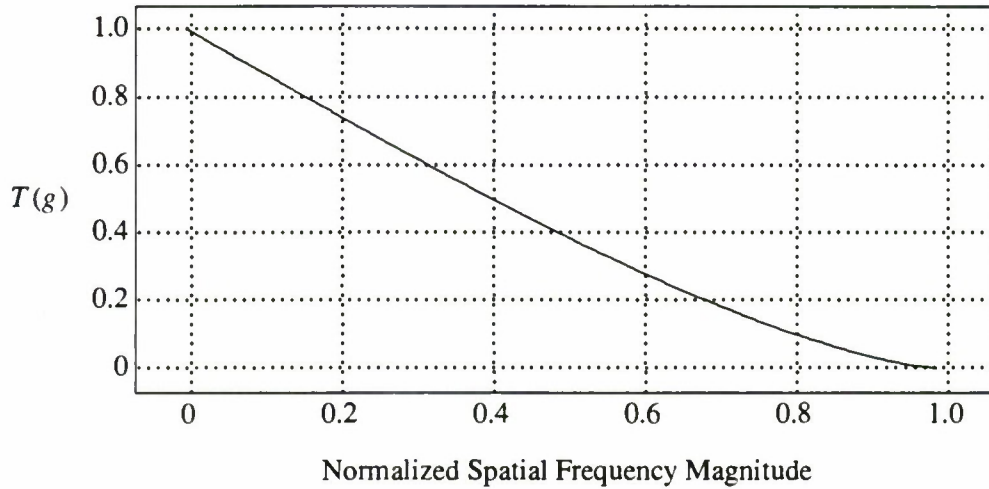


Figure 7.2. Circular aperture transfer function.

We can obtain the effect of this matched filter from the graph for a given scenario. For example, assume that we have a 1.0 m telescope, and that  $r_o$  is 10 cm. Then  $N(0)$  is  $(D/r_o)^2$  or 100. Figure 7.3 depicts some idealized curves for various situations. In the lower left, we start with a 10 cm telescope imaging some object with maximum S/N of some arbitrary value "R." If we increase our aperture to 1 m, we obtain a S/N which is  $100^2$  (40 dB) greater for the 0 spatial frequency. These two curves are just rescaled logarithms of Figure 7.2.

The top curve in Figure 7.3 illustrates perfect integration and is just a stretched version of the simple 1 m telescope curve. The theoretical speckle curve shows that below the seeing limit coherent combination occurs and we follow the simple 1 m telescope curve. The spatial frequencies beyond the seeing limit (i. e., normalized frequency 0.1) are noncoherently integrated. Note the resemblance to the speckle MTFs obtained by Korff and depicted in Figure 6.2. Unfortunately we must estimate these spatial frequencies using periodograms, which reduce the S/N to unity for a single image as shown in the bottom curve. When the seeing limit is exceeded, higher frequencies are limited to unity S/N until we are so near the diffraction limit that further decreases occur.

The theoretical speckle curve is obtained by the following construction. Since the integration gain of the noncoherent speckle process is the square root of the coherent gain of the 1 m perfect integration curve, we take half this distance on the log scale. Since we have an offset of R dB, the speckle curve lies halfway between the top curve and the line  $y = R$ . Where the simple 1 m telescope curve exceeds this value, we follow that curve instead.

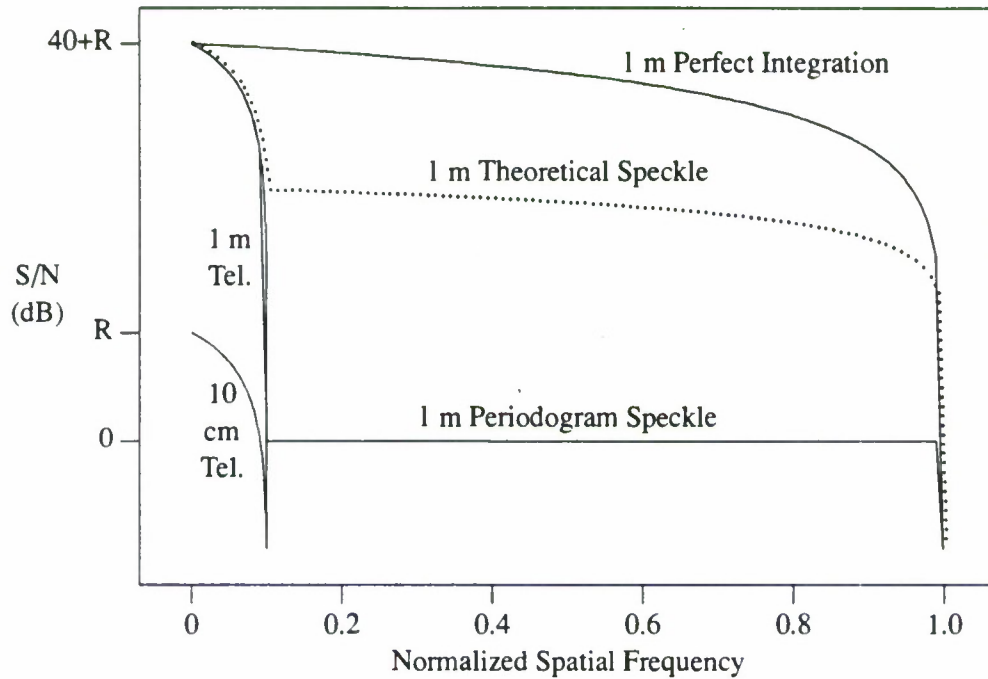


Figure 7.3. Effects of coherent integration.

Let us take a numerical example, say at  $g$  of 0.5, well beyond the seeing limit.  $T(g)$  here is 0.39 which implies that  $N(g)$  is 3900 (36 dB) in the coherent case and the square root of this quantity (62 or 18 dB) in the noncoherent case. The advantage of coherent integration is evident.

The loss in S/N in going from the theoretical speckle curve to the periodogram speckle case depends on the value of  $R$ . If  $R$  is small enough (below 0 dB) there may be very little loss. This is synonymous with short integration times, which are desirable for speckle anyway since they provide the best speckle transfer function.

### 7.2.3 Adaptive Wavefront Sensing

If an adaptive matched filter is being used, obviously real-time wavefront sensing and processing are needed. The wavefront detector shown in Figure 7.1 would presumably split off some light to an interferometer arrangement which would then be converted to wavefront modifier drive signals in the processor. Section 5 has adequately discussed compensated imaging. We will make a few remarks about new directions in adaptive systems and their possible application.

Compensated imaging typically uses light reflected from the target for turbulence sensing. An alternative theoretically permitting the imaging of fainter objects is to use some bright reference source. A bright star is the first thing that comes to mind, and indeed one is shown in Figure 7.1, but there is an extreme shortage of such stars.

An alternative is to use a so-called artificial star created by directing laser light at certain layers of the atmosphere. For example, experiments have been performed<sup>26</sup> using the sodium layer at about 90 km altitude. Adaptive optics require a reference which is unresolvable by a subaperture. Since a subaperture is on the order of  $r_o$  in diameter, Thompson and Gardner<sup>26</sup> maintain that the angular extent of an artificial star for this purpose should be about 1 arc sec. Smaller extents produce less light, degrading adaptive performance due to simple S/N considerations. Larger extents degrade adaptive performance as the reference is partially resolved by the subapertures.

Future adaptive optics systems will likely operate digitally from the interferometer intensity detectors through the processor. D/A converters will then drive the wavefront modifier circuitry. Digital operation implies segmentation of time rather than continuous calculation as in the analog approach. This segmentation is compatible with an operating mode in which a reference star is switched on and off and the wavefront sector synchronously samples data only when reference light is entering the instrument. Such a mode will probably be necessary to avoid contamination of the image data by the broadband reference star light.

#### 7.2.4 Spectral Filter

The adaptive optics components depicted in Figure 7.1 are assumed to work in white light. Hence it seems logical to image in white light as well. However, we are assuming that speckle techniques may be used to post-process the data and enhance it. We thus need to satisfy the speckle bandwidth restrictions discussed in Section 6.3.3.

The exact bandwidth of this filter is problematical. We have suitable guidelines for non-adaptive systems, although the optimum bandwidth does depend on the seeing. In this application optimum bandwidth depends on the seeing and also on the performance of the adaptive components of the instrument. The adaptive equipment *in some cases* may be considered to convert a small  $r_o$  into a much larger one, permitting a substantial relaxation of the bandwidth restrictions.

The ideal situation would be to divide the spectrum into multiple bands, recording each band. One could then make the decision during the data reduction process. Experience with a real system would doubtless lead to guidelines permitting suitable filter selection even without multiple spectral bands.

#### 7.2.5 Image Detector

New photon-counting detectors<sup>62,63</sup> are becoming available. These have major advantages for use in collection of data which may be enhanced with speckle techniques. The most obvious advantage is that the integration interval can be determined during data processing rather than before collection. This gives the user the chance to optimize this parameter in every case; it is particularly useful in the satellite imaging case where we have already noted that unique events are common.

Another obvious advantage of photon-counting detectors is that the data are recorded digitally. This saves a lot of tedious and expensive digitization. For dim objects the volume of data can also be reduced.

We have noted that it is advantageous to select bandwidth and integration time after the data are collected. It seems that what is really needed is a color photon-counting camera which records photon  $x$  and  $y$  coordinates, arrival times, and some measure of wavelength. This would provide maximum flexibility and the potential for either true color images or improved S/N.



The method of producing color images is obvious. Improving S/N relies on the likelihood that most objects have similar spatial frequency distribution over a substantial range of wavelengths. If this is the case, the S/N could be increased by combining images from various color bands. A scaling correction for the magnification factor would probably be necessary.

#### **7.2.6 Post-Processing**

Any system has its imperfections, and despite our analysis of the wavefront corrector as a perfect matched filter, there will be certain degradations in the image received by the detector. For example, the photon noise associated with the finite number of photons received in each subaperture will produce some error in the differential wavefront tilts. The calculation of the wavefront modifier weights will involve some error.

This adaptive system is a feedback control system. All such systems work by sensing errors at the output of the system and driving the system in such a way as to reduce those errors. The magnitude of the residual error depends on the feedback loop gain, but the point is that zero error is never achieved.

There are also physical effects such as scintillation. We are modifying only the phase of the received wavefront, so errors in the amplitude remain, although those are of course much smaller. We discuss these errors in more detail below.

A more fundamental problem is the problem of isoplanicity. An adaptive system containing a single wavefront modifier operates correctly only over some isoplanatic angle of perhaps several arc seconds. Targets which subtend more than this angle will be imaged with errors contributing to a loss of resolution.

Much of the theory of speckle imaging looks applicable to the problem of post-processing data which has been adaptively processed. There will be differences between straight speckle processing and speckle post-processing of adaptively corrected data, and theoretical work remains to be done.

If adaptive errors can be statistically characterized, combining multiple images in the speckle tradition seems potentially able to reduce those errors and produce improved images. This approach seems more fruitful and more true to the physics than the blind application of image processing techniques to filter out noise or enhance edges. Wiener filtering of individual frames is likely to be inferior to techniques based on multiple frames. In the case of a lack of isoplanicity, Wiener filtering is not even theoretically applicable.

The isoplanicity problem is one area in which post-processing may improve things. There is no obvious way to deal with this problem in the adaptive framework with a single wavefront modifier and still image objects subtending large angles. However, one might be able to divide a speckle image into sectors, performing speckle processing on each sector individually.

In sum, there is no shortage of possibilities for post-processing. We will discuss some of these ideas further later in this section.

### **7.3 SPECIAL PROBLEMS OF SATELLITE IMAGING**

We have already alluded to some of the problems of satellite imaging as compared to astronomical imaging. Next we will discuss these in more detail.

### 7.3.1 Satellite Motion

Low-earth-orbit satellites suitable for optical imaging typically pass over the telescope rather rapidly. One implication of this is that high performance trackers are needed to keep the telescope pointed at the target. We will not consider that issue any further, but it is a major hardware consideration.

Another implication which concerns us is the limited length of the available image sequence. Regardless of the satellite motion, during the twilight hours suitable for imaging we expect to collect data for only several minutes. This is substantially less than the tens of minutes or hours often used in speckle data collection. We have a potential S/N problem; the coherent integration provided by wave-front compensation could be mandatory here for imaging certain objects.

Modern high-resolution optical techniques are quite effective in astronomy in which most objects of interest appear to be two-dimensional objects attached to the “celestial sphere.” Rotations about the line-of-sight (LOS) are easily removed from the data.

In satellite imaging, we image three-dimensional objects whose rotation in general is not about the LOS. We cannot correct for the component of motion not about the LOS so unavoidable blurring is produced. This effect further limits the length of data which we can integrate.

We would like to know how long we can expect to integrate data for speckle processing. We are trying to gain resolution through speckle integration but we are losing some resolution through blurring. We can calculate this effect for a given example with some simplifying assumptions to provide insight into the problem.

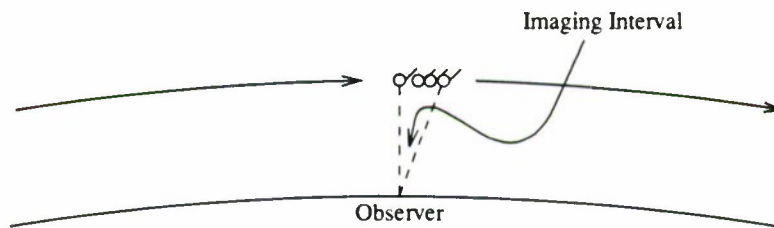


Figure 7.4. Satellite imaging geometry.

Consider the geometry of Figure 7.4. Assume that we are imaging a satellite in a circular orbit of 300 km which passes directly over the observing site. The orbital period is 90.5 min, which gives a target velocity of about 7.7 km/s. When the target is directly overhead, the angular rate of change is  $1.48^\circ/\text{s}$ .

We will image starting at the zenith for some interval as shown. The satellite being imaged consists of a featureless cylinder, the cross-section of which is shown in the figure, and a square solar panel inclined at some angle  $\theta$  with respect to broadside. We are interested in high-resolution imaging of this solar panel. Even if the panel is tracking the sun, we expect very little angle change over the short imaging interval, so we will assume that  $\theta$  changes only due to the change in viewing angle from the ground.

Assume further that we are using a 2 m telescope, which at 500-nm wavelength gives us a diffraction-limited resolution of about 0.05 second of arc. Let the field of view of the telescope be 10 m,

and the dimension of the solar panel be 5 m. Assume that the blurring effect is due to foreshortening of the panel as its angle changes in the x direction, as shown in Figure 7.5. Note that there is no blurring in the y direction in this example. We assume in Figure 7.5 that  $\theta$  is  $40^\circ$  at zenith, and increases to  $50^\circ$  over a potential  $10^\circ$  imaging interval.

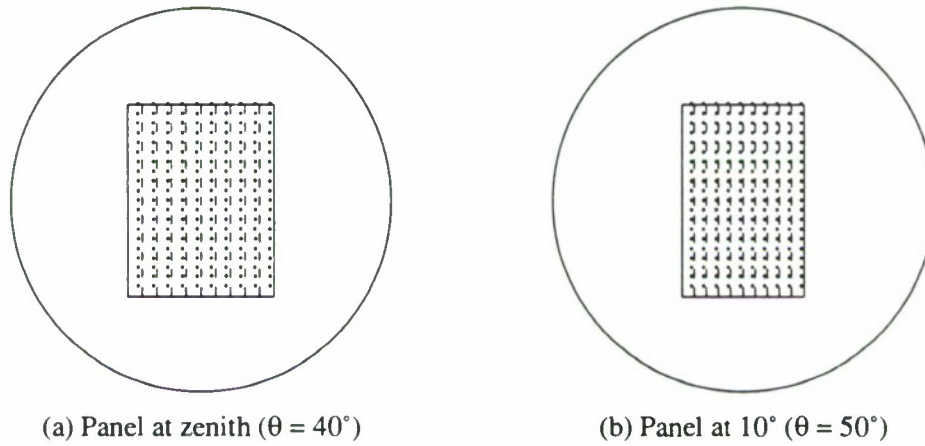


Figure 7.5. Imaging a solar panel.

The effect of this foreshortening on imaging is easy to determine approximately. If the effective width of the panel changes 10 percent over the imaging interval, then spatial frequencies beyond about 10 cycles over the panel are lost. At that point, things are completely out of phase from one side of the panel to the other.

In our example, the angular extent of the solar panel at zenith is about  $(5 \text{ m})(\cos 40^\circ)/(300 \text{ km})$  or  $2.6''$ . The diffraction-limited maximum spatial frequency is then about  $2.6/.05$  or 52 cycles/panel. Clearly we can tolerate something like 2 percent foreshortening.

Figure 7.6 shows curves of integration time vs spatial frequency limit measured as a fraction of the diffraction limit. Remember that the diffraction limit in cycles/meter for the panel depends on its orientation, being a maximum at broadside. We can see that if we confine our integration to about 0.85 s blurring will not limit our resolution. If we go to 2 s to improve the S/N, we lose more than half our potential resolution. The situation gets better for smaller  $\theta$  as shown; it also gets worse for larger  $\theta$ .

An actual satellite is more complicated than the simple model analyzed here. It is likely in practice that many different surfaces of the satellite will be at different viewing angles. Hence blurring will affect different surfaces differently. This type of analysis can be used in interpreting the results of integrated optical imagery by considering portions of the object. This is particularly easy if a good motion solution is available.

### 7.3.2 Bistatic Imaging

In the case of imaging distant astronomical objects, we may consider them fixed to the celestial sphere. That is, we are at the center of the celestial sphere so a given object always looks the same,



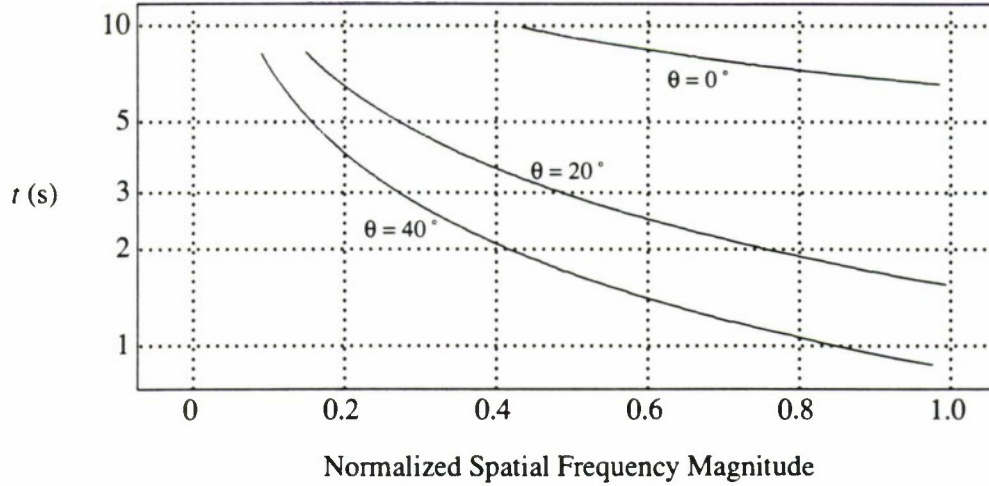


Figure 7.6. Maximum integration time for specified resolution.

except for a rotation. Hence a single parameter describes the family of images that we can obtain. We also know what the rotation is, so it is easy to correct.

If the receiver and transmitter of an imaging system are co-located, we are performing monostatic imaging. This is the case in radar, for example. When imaging a three-dimensional object we can characterize the possible views of that object by imagining the *object* to be at the center of a large sphere. As we move around the outside of the sphere, we obtain different projections of the object. Hence two additional parameters “latitude and longitude” join the single rotation parameter to characterize the space of possible images.

Optical imaging with solar illumination is a bistatic process. If the object is inside a sphere as in the monostatic case, the receiver (telescope) is at some coordinate pair and the transmitter (sun) is at another one. Due to symmetry, rotations of the sun are not important. Hence rather than having three coordinates specifying the orientation of the satellite we have five; three specifying the satellite and two specifying the sun!

Low-earth-orbit objects can be successfully optically imaged just before sunrise and right after sunset. A stable satellite at a given elevation would experience solar illumination from the east in one case and from the west in the other. This would cause different shadowing effects. On a given day or week there would be essentially two illumination angles for a given satellite orientation, but throughout the year these angles would be changing. In addition, reflections from the earth affect the image. These are somewhat dependent on weather, season, etc.

In summary, when speckle imaging or speckle post-processing adaptive images of astronomical objects, all of the data can be potentially combined if the (known) rotation is removed from the data. When satellites are imaged, the data collected must be processed in subsets characterized by up to five parameters. Two of those parameters are known; the satellite orientation (motion solution) may also be known through independent means such as radar imaging. If it is not, the problem of determining the three-dimensional model of the satellite being imaged is made more difficult.

We are trying to characterize a three-dimensional object using a number of two-dimensional images. The number of such images is greater in the bistatic imaging case. This can have the effect of reducing the amount of data available for integration. If this S/N issue is not a problem, we will have greater potential information content as well as a greater challenge to extract that information.

### 7.3.3 Field of View

We have already discussed the problem of nonisoplanicity in Section 6.3.4. The examples there show that objects subtending more than several arc seconds will suffer from nonisoplanatic effects which tend to reduce resolution.

It would not be unusual in optical space surveillance to be viewing a satellite at a range of 300 km which is 10 m in some dimension. In this case, the corresponding angular extent is 6.9"! This is particularly a problem for wavefront compensation, since as we have discussed speckle processing suffers a loss of S/N but still has the potential of recovering through integrating more data.

## 7.4 ANALYSIS OF SMALL AMPLITUDE AND PHASE ERRORS

Since we expect an adaptive feedback system to retain certain small errors, it is natural to ask what the effect is of such errors. The simplest way to characterize the error is to determine its effect on the system MTF. Indeed, corrections for the MTF are normal in speckle processing.

To gain intuitive appreciation for what is going on, a simple-minded simulation of turbulence was produced in which the phase standard deviation  $\sigma_\phi$  could be selected. While the rectangular phase error spectrum generated was not as realistic as possible, we expect the effect of small errors on the MTF to be qualitatively realistic. The results were as shown in Figure 7.7. The simulation is performed in one dimension, for various values of  $\sigma_\phi$ . The curve appears to be similar to a constant plus a  $\sin x/x$  at the origin.

Compensated imaging corrects the phases in a feedback loop, and as discussed above there are several reasons why it cannot correct them perfectly; that is why the simulation modeled phase errors. But recall from our discussion of turbulence that there is always some scintillation in the magnitudes as well. Roddier and Roddier<sup>64</sup> published an analytical analysis using certain approximations of the effect on the OTF of uncorrected amplitude errors due to scintillation. The curves which resulted look almost the same as Figure 7.7!

To understand why that is so, we will return to Goodman.<sup>4</sup> His "Gaussian random-phase screen" analysis is equivalent to our phase error scenario. This screen introduces a specified random phase shift in the pupil plane of an imaging system without disturbing the amplitude of the wave.

The analysis is similar to our previous discussions about the interferometric view of imaging. The OTF of the screen is the spatial autocorrelation function of its amplitude transmittance function. The results shown by Goodman are again very reminiscent of Figure 7.7. We can easily understand how these similarities arise by recourse to communications theory.

In the theory of modulation, amplitude modulation with carrier (AM) and narrowband phase modulation (PM) are two well-analyzed techniques discussed in any elementary textbook, such as Lathi.<sup>65</sup> In the communications context, a sinusoidal carrier at frequency  $\omega_c$  is modulated by an information signal

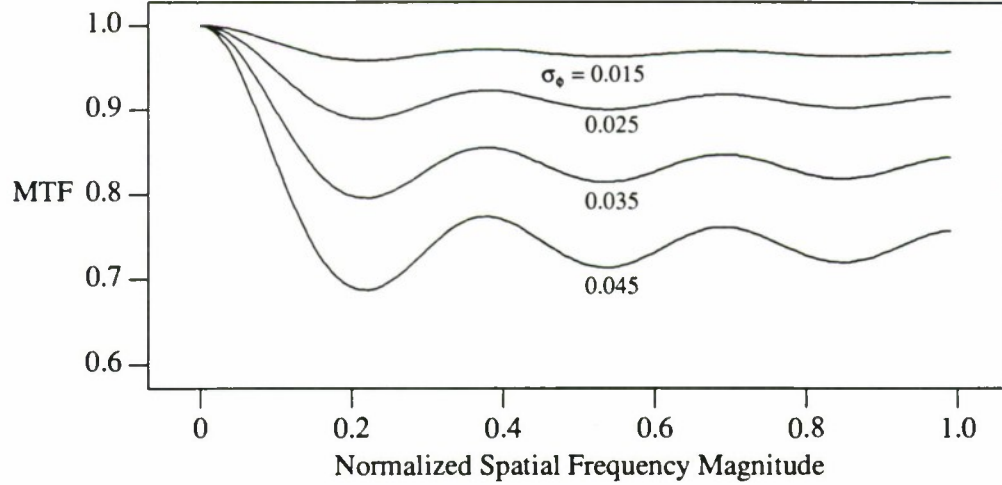


Figure 7.7. Simulated MTF of random phase errors.

$f(t)$  for the purpose of transmitting  $f(t)$  to a receiver. In the case of AM, the transmitted signal is

$$f_t(t) = [A + f(t)] \cos \omega_c t \quad (7.2)$$

and in the case of PM,

$$f_t(t) = A \cos [\omega_c t + k f(t)]. \quad (7.3)$$

The constant  $k$  is known as the modulation index.

To couch our optical problem in the language of modulation theory, let the amplitude  $A$  be unity, let  $\omega_c = 0$ , and replace the time function  $f(t)$  by some spatial error function  $f(x)$  of either amplitude or phase. We then model the spatial signal with amplitude errors as

$$1 + f(x) \quad (7.4)$$

and the signal with phase errors as

$$\cos [f(x)]. \quad (7.5)$$

We are interested in the autocorrelation functions of these expressions. The simplest way to obtain them here is to first compute the power spectrum, and then Fourier transform (FT). We can appeal to well-known results of modulation theory rather than doing any calculations ourselves.

The AM analysis is fairly trivial; clearly the power spectrum of Equation (7.4) consists of an impulse at the origin plus the power spectrum of the modulating signal, say a Gaussian. Its FT is a constant plus the FT of a Gaussian, which is also Gaussian.

While generalized PM is rather difficult to analyze, involving numerous Bessel functions, the special case of narrowband PM is much easier. Since we assume small phase errors, we satisfy the narrowband restriction that  $k f(t) \ll \pi/2$ . It turns out that the FT of a narrowband PM signal is similar to



the FT of an AM signal. The only difference is that the sideband components are multiplied by a scale factor of  $jk$ , which amounts to a phase shift of  $\pi/2$  and a scaling by the modulation index.

We conclude the power spectrum is the same as in the AM case, apart from scaling, so we have explained the qualitative similarity in the OTF due to small phase errors and small amplitude errors. We also have obtained additional insight into the exact form of the OTF of small errors. If we can determine the power spectrum of those errors, the FT of that spectrum added to a constant is the desired OTF.

Looking back at the three examples which inspired this analysis, our simulation has a rectangular power spectrum which generated a  $\sin x/x$  autocorrelation function. This accounts for the ripples in Figure 7.7. The scintillation paper<sup>64</sup> also shows ripples which reflect the spectrum of the amplitude errors. Goodman<sup>4</sup> uses a theoretical Gaussian, so his curves show no ripples.

## 7.5 SELECTING A PHASE-RETRIEVAL ALGORITHM

Post-processing of data based on speckle techniques boils down to selecting a phase-retrieval algorithm. We have a number of spatial frequencies below the seeing limit (or below the adaptive correction limit) whose phase is correct. Higher spatial frequencies which we desire to retrieve have phases which are essentially uncorrelated with the corresponding spatial frequency phases of the object. We have either a good idea of the magnitude of these frequencies, differential phase information, or both. The problem is to determine the missing phases from the available information.

As we have discussed previously in Section 6, there are two basic approaches to the problem, phase retrieval from magnitude such as Fienup's method, and integration of differential phases such as Knox-Thompson or triple correlation. We have not provided much guidance previously about which methods to use.

The answer lies in the well-known axiom<sup>66,67</sup> of image processing that the phase is much more important than the magnitude. Even with no magnitude information, or the magnitudes of another image, an image can be recognized. On the other hand, with only magnitude information the image is not recognizable.

We are really estimating both the magnitude and the phase of an image before we display it. What the importance of phase tells us is that we should probably spend less time worrying about errors in the magnitude since errors in the phase are much more important.

If we have copious views of reference stars either with very little angular separation from the object being imaged or as part of a very large data set, we may feel that our estimate of the magnitudes using Labeyrie's method is quite good. In that case, following with Fienup's method is probably a reasonable option. Unfortunately, that is probably *not* the case in most satellite imaging.

If we have substantial uncertainty in the magnitudes due to a short data set with little suitable reference data, we should be reluctant to base a Fienup reconstruction on those magnitudes. On the other hand, doing our best job with one of the differential phase algorithms lets us essentially ignore the magnitude problem. We expect that if we get good phases, the image will contain detectable detail in those spatial frequencies even in the face of poor magnitude estimates. We can then work on improving the magnitudes without affecting the phases.

## 7.6 OPTICAL DATA RESOLUTION EVALUATION

The basic idea of optical data resolution evaluation is to determine the quality of high-resolution optical data. There are several reasons why this quality may be uncertain. Since the parameters of speckle imaging depend on the seeing conditions and the nature of the object being imaged, and we have only limited knowledge of these conditions, even the best-planned measurement program has some uncertainty. If we are post-processing existing data taken under less controlled circumstances or with inferior equipment, the uncertainty will increase greatly. This situation might occur for example if we plan to post-process data taken by an adaptive optics system or with a camera of poor quality.

Not all objects contain significant energy at the higher spatial frequencies. At some frequency which depends on the object spectrum, the object energy drops below the noise. Space objects may be rotating and introducing an unknown blur which affects the high frequencies first. These uncertainties remind us of our discussion of reference stars in Section 6.1.2.2. We assume here that there is no handy reference star so the data must be evaluated using internal evidence.

Assume we are evaluating a set of  $n$  consecutive speckle images  $i_n(x,y)$  taken at a usefully short exposure time. We first compute the DFTs of the images  $I_n(u,v) \equiv I_n(\mathbf{f})$ . We would like to know which spatial frequencies are present and contributing to the existing image quality. We then want to go on to determine which differential spatial frequency phases are present and suitable for speckle phase recovery. These two measures are functions of the magnitude of vector spatial frequency  $|\mathbf{f}|$ , so we will average both measures over rings of constant  $|\mathbf{f}|$  in the spatial frequency plane to smooth the estimates.

It might be argued that the first measure is sufficient; to determine the speckle improvement potential we could simply perform the speckle processing and then re-evaluate the data using the first quality measure. The reason for proposing a measure of speckle potential is to avoid a possibly expensive and complicated phase recovery operation. The goal is to obtain a relatively simple and sensitive indication of potentially recoverable spatial frequencies which could guide speckle phase recovery experiments. We can also perform constant  $|\mathbf{f}|$  averaging which is not applicable to image phase recovery; this may improve sensitivity and enable us to obtain a better estimate of spatial frequency content as a function of  $|\mathbf{f}|$ .

We adopt the following approach to the problem:

- (a) Since Fourier phases are more important to image quality than magnitudes, we base our image evaluation on DFT phase statistics.
- (b) Speckle enhancement potential is based on the statistics of differential DFT phases.
- (c) Each image quality measure is a one-dimensional function of spatial frequency resolution or potential resolution.
- (d) Since we do not know the true object phases or “ground truth,” we partition the data into two or more disjoint subsets and examine correlations within the data. Closely correlated phases are assumed to correspond to true object phases.

We may make use of magnitude information in computing these phase measures. For example, using only frequencies whose magnitudes exceed the ring median or weighting the contributions would probably improve performance.

## 7.6.1 Basic Image Quality Measure

### 7.6.1.1 Definition

Our basic image evaluation function  $s_{\phi}^2(|\mathbf{f}|)$  is straightforward. We start with the assumption that if the rms spatial frequency phase error  $\sigma_{\phi}$  is small (perhaps less than  $2\pi/10$ )<sup>44</sup> for some frequency  $\mathbf{f}_k \equiv (u_k, v_k)$ , we are getting reasonable benefit from that spatial frequency. Since we don't know the true phases, we partition the data into two subsets and consider some function of the phase difference at each spatial frequency as an indication of the mean squared error produced by averaging the total data set. We then average over frequencies for which  $|f - f_k| < \Delta$  (rings) to obtain a one-dimensional function of  $|\mathbf{f}|$ . If we choose the *average squared phase differences* as our phase difference function we are computing

$$\frac{1}{N_{\mathbf{f}_k}} \sum_{|\mathbf{f} - \mathbf{f}_k| < \Delta} [\bar{\phi}_1(\mathbf{f}) - \bar{\phi}_2(\mathbf{f})]^2 \quad (7.6)$$

where  $N_{\mathbf{f}_k}$  is the number of discrete frequencies within  $\Delta$  of  $\mathbf{f}_k$  and  $\bar{\phi}_i(\mathbf{f})$  is the average phase of set  $i$  at frequency  $\mathbf{f}$ .

A more general approach is to use the *sample phase variance*; this allows us to generalize by dividing the data into more than two sets. Dropping the bars for notational simplicity, the squared phase difference is

$$(\phi_1 - \phi_2)^2 = \phi_1^2 + \phi_2^2 - 2\phi_1\phi_2 \quad (7.7)$$

while the sample phase variance for  $K$  samples is

$$s_{\phi}^2 = \frac{\sum_{i=1}^K (\phi_i - \bar{\phi})^2}{K-1} \quad (7.8)$$

where  $\bar{\phi}$  here is the mean of the  $K$  samples. For the case  $K = 2$ ,

$$s_{\phi}^2 = \frac{\phi_1^2}{2} + \frac{\phi_2^2}{2} - \phi_1\phi_2 \quad (7.9)$$

which is just half the squared phase difference.

Using the sample variance approach with  $K = 2$ , we obtain the image evaluation function  $s_{\phi}^2(|\mathbf{f}|)$

$$s_{\phi}^2(\mathbf{f}_k) = \frac{1}{N_{\mathbf{f}_k}} \sum_{|\mathbf{f} - \mathbf{f}_k| < \Delta} \left[ \frac{\bar{\phi}_1^2(\mathbf{f})}{2} + \frac{\bar{\phi}_2^2(\mathbf{f})}{2} - \bar{\phi}_1(\mathbf{f})\bar{\phi}_2(\mathbf{f}) \right]. \quad (7.10)$$

For this function, there is nothing to be gained by averaging many image DFTs to obtain the  $\bar{\phi}$  functions. As our previous notational simplification suggests, simply using two images separated by perhaps 30 ms to 1 s should be quite suitable. This will not be the case when we discuss the speckle potential functions below.

We expect  $s_{\phi}^2(|\mathbf{f}|)$  to look something like Figure 7.8. There is small phase difference until we approach the seeing limit, at which time there is rapid increase to some limit. We can say something



about that limit in the case in which the two subsets have only a single image each. If the two images do not overlap in time, *and we are in the noise regime or beyond the seeing limit*, we expect the spatial frequency phases to be uncorrelated. If the noise is Gaussian, the phases will be jointly uniformly distributed, and the density function will be constant within the bounds of Figure 7.9(a). Taking the expected value of Equation (7.9),

$$E[ s_{\phi}^2(|f|) ] = E \left[ \frac{\bar{\phi}_1^2(f)}{2} + \frac{\bar{\phi}_2^2(f)}{2} - \bar{\phi}_1(f) \bar{\phi}_2(f) \right] \quad (7.11)$$

$$= E[ \bar{\phi}_1(f)^2 ]$$

since the phases are uncorrelated. This is the variance of a uniformly distributed random variable over the interval  $[-\pi, \pi]$  which is  $4\pi^2/12$  or about 3.29. We will defer further discussion of this limit to the next section.

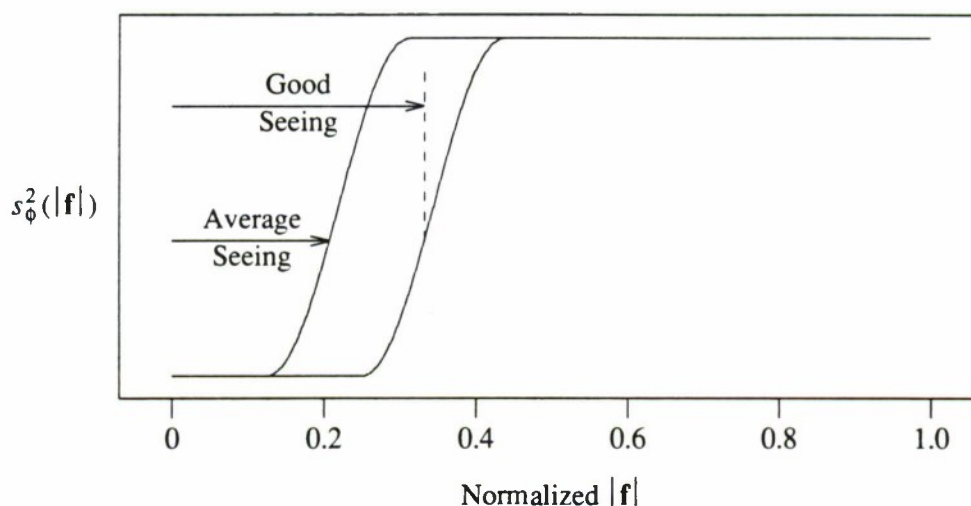


Figure 7.8. Typical image evaluation functions.

### 7.6.1.2 Problems of Phase Discontinuities

When we compare phases for purposes of computing the sample phase variance, we take out  $2\pi$  discontinuities for obvious reasons. We can view this process as conditionally adding or subtracting  $2\pi$  to the second random variable. The joint density function now is constant within the boundaries of the function depicted in Figure 7.9(b). This operation evidently produces correlated random variables. The cross term of Equation (7.11) now is not zero, and we must integrate to determine the expected value of this two sample variance. This straightforward calculation produces  $\pi^2/2 - \pi$  or about 1.79.

As mentioned above, we can successfully compute  $s_{\phi}^2(|f|)$  with just two images in which case the above analysis is appropriate. When we consider more than a single image per data set, which is

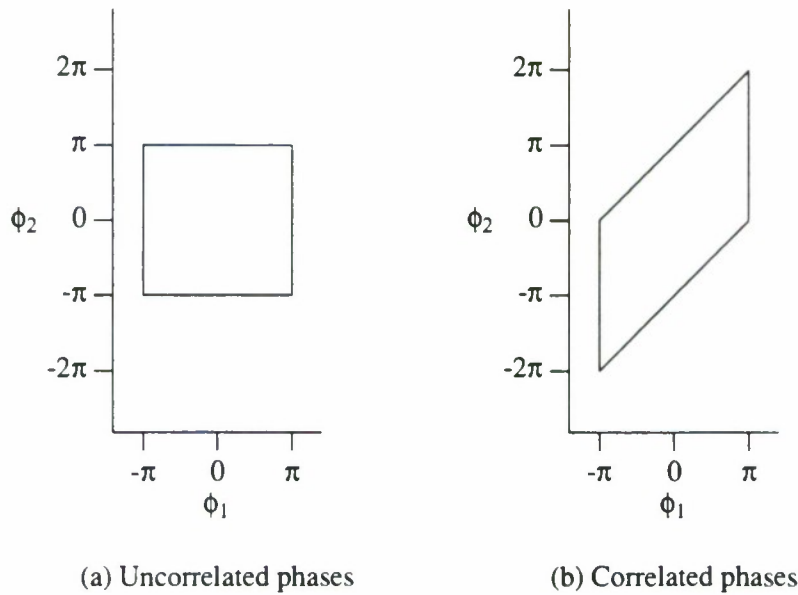


Figure 7.9. Joint probability density functions of  $\phi_1(\mathbf{f})$ ,  $\phi_2(\mathbf{f})$ .

essential for the differential phase function described below, things get more complicated. We would like to take out the phase discontinuities in the averaging process for each set. Determining the optimum set of  $2\pi$  additions and subtractions which minimize the variance of a set of data is a non-trivial optimization problem. We could handle it, but doing it for each spatial frequency in a large image might be burdensome. The analysis of such a process might also be rather difficult.

If we proceed using a simple ad hoc generalization of our procedure for removing a single discontinuity from two samples, we probably obtain near-optimum results. The analysis is also straightforward, although very tedious. A sequence of two-dimensional integrations is required to analyze the effect of this process for white noise. Simulating  $n$  random images indicates that  $\sigma^2$  increases from about 4.1 to 5.4 as the  $n$  goes from 2 to 50. The distribution rapidly approaches a Gaussian as one might expect.

Of course our ad hoc discontinuity removal process is not completely defensible when dealing with a Gaussian distribution rather than a uniform one. A Gaussian distribution with  $\sigma^2$  of 5.4 has  $\sigma$  of 2.32, which means that  $\pm\pi$  occurs at about  $1.35\sigma$ . Only 18 percent of the density exceeds this value, and the density has fallen to 40 percent of the uniform density level at the edges. This is not so far from uniform as to introduce major deviations from the two image case; indeed simulations show that the limiting value of  $s_\phi^2(|\mathbf{f}|)$  remains fairly close to 1.8 when multiple images are processed.

If we omit the discontinuity removal altogether, then random phases experience variance reduction proportional to the number of phases averaged. Hence the expected distribution becomes a Gaussian with smaller and smaller variance. This processing itself is not suitable for a general purpose data evaluation function due to its asymptotic sensitivity to the exact numbers of images processed. We have the

undesirable behavior in which the limiting value signifying the diffraction limit or the end of useful information varies. There are perhaps ways to deal with this difficulty, but phase discontinuities would degrade performance so it doesn't seem worth pursuing.

### 7.6.1.3 Interpreting the Function

From this analysis it follows that  $s_{\phi}^2(|\mathbf{f}|)$  should start very small for small spatial frequencies below the seeing limit. It should increase fairly rapidly at the seeing limit to an asymptotic value around 1.8 as shown in Figure 7.8. If the data are extremely noisy, or the object has few significant spatial frequencies beyond some point, the slope of the increase may be more gradual and the initial increase may occur earlier. Any values of  $s_{\phi}^2(|\mathbf{f}|)$  significantly below 1.8 suggest some spatial frequency phase information, but the contribution to image quality is suspect unless  $s_{\phi}^2(|\mathbf{f}|)$  is below 0.4 or 0.5. The image degradation due to phase errors depends on the object and on the magnitude errors as well.

If averaging occurs in rings of constant  $\Delta|\mathbf{f}|$ , the number of spatial frequencies averaged increases with  $|\mathbf{f}|$ . Hence we expect noisier estimates at lower  $|\mathbf{f}|$ ; simulation clearly shows this effect. Averaging in different-sized rings could compensate for this effect and produce smoother curves, although as long as the phenomenon is understood it is unlikely to cause much confusion.

## 7.6.2 Speckle Potential Evaluation

### 7.6.2.1 Phase Difference Approach

The  $s_{\phi}^2(|\mathbf{f}|)$  function is relatively easy to compute and analyze; the phases are never extremely far from a uniform distribution and the lower frequency phases are very well correlated. We next tackle the more difficult problem of detecting speckle-recoverable phases.

The idea behind the speckle potential evaluation is to compute phase differences with some small offset in the frequency plane in the same way some of the phase recovery algorithms work. Rather than doing anything with the phase differences, we just statistically study them to determine the potential for phase recovery.

The most obvious approach is very similar to that for the  $s_{\phi}^2(|\mathbf{f}|)$  function, with DFTs of short-exposure images furnishing the raw data. However, instead of using the phases of the spatial frequencies we first compute the differences of spatial frequency phases separated by one frequency step in  $u$  and one in  $v$ . The remaining processing follows the same way as before. We average a number of frames to form two or more sets of average differential phase. We then compute the sample variance for each spatial frequency.

$$s_{\Delta\phi}^2(\mathbf{f}_k) = \frac{1}{N_{\mathbf{f}_k}} \sum_{|\mathbf{f}-\mathbf{f}_k| < \Delta} [\Delta\Phi_1(\mathbf{f}) - \Delta\Phi_2(\mathbf{f})]^2. \quad (7.12)$$

In Figure 7.10 we show the functions  $s_{\phi}^2(|\mathbf{f}|)$  and  $s_{\Delta\phi}^2(|\mathbf{f}|)$  calculated using two sets of 10 simulated monochromatic speckle images of a point source. The MTF is simulated to roll off linearly to zero at the diffraction limit, at which point only noise contributes to the phases. In the limit of completely uncorrelated signals,  $s_{\Delta\phi}^2(|\mathbf{f}|)$  behaves the same as  $s_{\phi}^2(|\mathbf{f}|)$ , and the asymptotic value of about 1.65 (due to the multiple images) is approached. All of our discussion of phase discontinuity removal, both in



averaging the differential phases and in computing the variance itself, applies. We see that  $s_{\Delta\phi}^2(|\mathbf{f}|)$  indicates speckle phase recovery potential quite near to the diffraction limit. We see greater fluctuations in the  $s_{\phi}^2(|\mathbf{f}|)$  curve for smaller  $|\mathbf{f}|$  as expected.

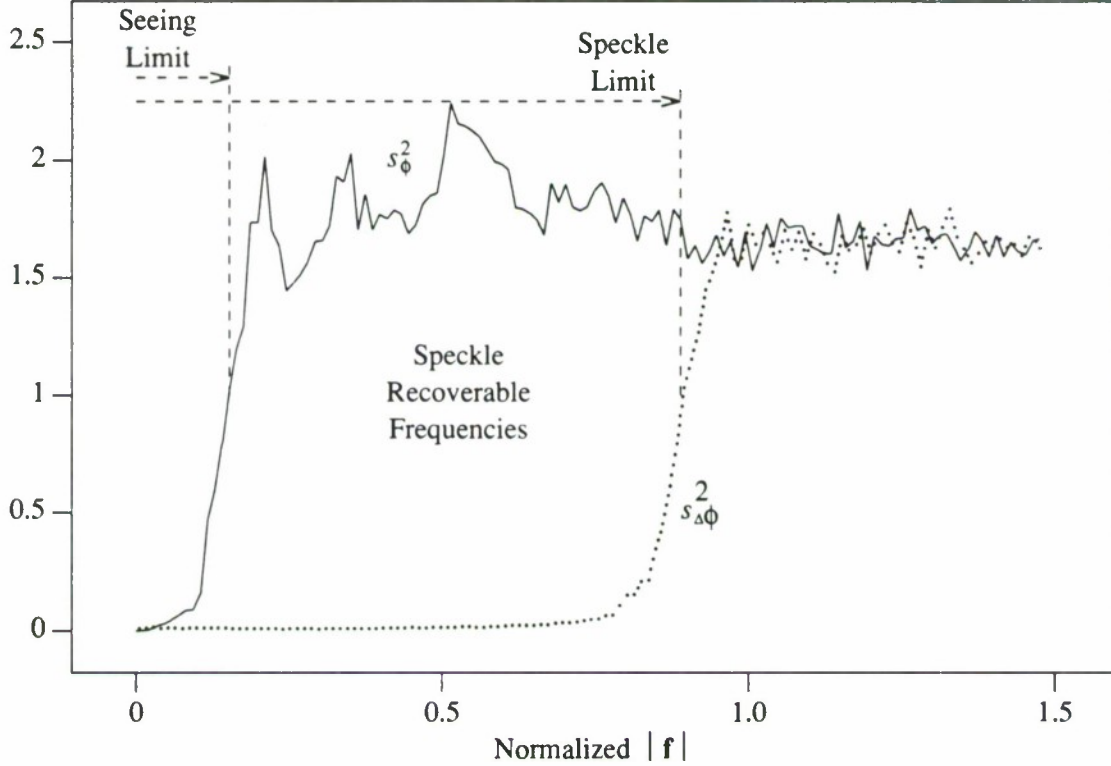


Figure 7.10. Evaluation functions for simulated data.

This works very nicely for simulated point sources but fails for realistic extended objects. The problem occurs with the spatial frequencies beyond the seeing limit and below the diffraction limit in which we have the most interest. The analysis producing the asymptotic value 1.79 assumes that the data are roughly uniformly distributed over  $[-\pi, \pi]$  and any phase discontinuities are removed. In the case of  $s_{\phi}^2(|\mathbf{f}|)$ , spatial frequencies beyond the seeing limit are indeed independent and uniformly distributed or close to it. However, this is not the case for the differential phase used to compute  $s_{\Delta\phi}^2(|\mathbf{f}|)$ .

To see this we can consider a simple model in which the object is a random field inside some defined region of the  $(x, y)$  plane and zero outside. Goodman and Belsher<sup>25</sup> define a similar model in which the support region is a square.

If we have a sample function of a random field, and we window it by some support function, that is equivalent to convolving its transform by the transform of the window, say a sinc function for a

rectangular window. The result is that significant correlations appear between neighboring frequencies in the DFT. It follows that differences of closely spaced frequencies are smaller than they would be otherwise. The differences are smaller in both the real and the imaginary parts of the complex FT, and hence the phase differences are also smaller.

We now have a phase distribution which is much narrower than a uniform on  $[-\pi, \pi]$ , so when we compute the variance for  $s_{\Delta\phi}^2(|\mathbf{f}|)$  we will automatically obtain smaller numbers. This is independent of whether or not the spatial frequency phase differences are correlated across the two data sets. Clearly the expected value of  $s_{\Delta\phi}^2(|\mathbf{f}|)$  in this region depends on the support region of the object as well as on the speckle processing potential. A larger support region will produce a smaller transform width and hence produce less frequency domain correlation.

We are saying that the phase function of a DFT is smooth due to the support constraints. This does not affect  $s_{\phi}^2(|\mathbf{f}|)$  since the smooth variation is random from data set to data set. It does, however, prevent us from easily detecting speckle-recoverable frequencies by just looking for frequencies whose differential phase variance is significantly below the asymptotic value.

### 7.6.2.2 Sample Correlation Approach

An alternate approach is based on sample correlation coefficients. To avoid sensitivity to the particular distributions, a sample correlation coefficient may be computed which will always lie between -1 and 1. We can select all of the frequencies in an averaging ring as samples; if they show phase correlation between the two data sets we expect a positive correlation coefficient. Incidentally, we are again restricted to partitioning our data into only two sets.

The use of correlation coefficients to estimate unknown signal and noise powers has been analyzed<sup>68</sup> previously for ordinary one-dimensional signals. We have a somewhat unconventional application for sample correlation coefficients. Normally we would expect to be given  $n$  sample pairs from two, possibly correlated, distributions. The number which best represents the strength of the linear relationship between the two distributions is given by

$$r = \frac{\sum_{i=1}^n (x_i - \bar{x})(y_i - \bar{y})}{ns_x s_y} \quad (7.13)$$

where  $\bar{x}$  and  $\bar{y}$  are the sample means, and  $s_x$  and  $s_y$  are the sample standard deviations.

We are proposing to apply Equation (7.13) to a set of sample pairs representing a number of discrete frequencies  $\mathbf{f}_i$  whose vector frequency magnitudes are within some  $\Delta$  of spatial frequency magnitude  $\mathbf{f}_k$ . The correlation we are looking for is between the data subsets. Omitting the limits on the sums and the explicit  $\phi$  dependence on  $\mathbf{f}$  and expanding we obtain the following function

$$r = \frac{n \sum \bar{\phi}_1 \bar{\phi}_2 - \sum \bar{\phi}_1 \sum \bar{\phi}_2}{\left[ [n \sum \bar{\phi}_1^2 - (\sum \bar{\phi}_1)^2] [n \sum \bar{\phi}_2^2 - (\sum \bar{\phi}_2)^2] \right]^{1/2}} \quad (7.14)$$

in a form suitable for machine evaluation. Since we know that the phase means should be zero, we can explicitly include that knowledge to obtain the final expression

$$r_{\Delta\phi}^2(\mathbf{f}_k) = \frac{n \sum \bar{\phi}_1 \bar{\phi}_2}{\left[ n \sum \bar{\phi}_1^2 \ n \sum \bar{\phi}_2^2 \right]^{1/2}}. \quad (7.15)$$

In cases where only a few phase samples are included in the sums, this provides a substantially more robust estimator of correlation.

Figure 7.11 shows  $r_{\Delta\phi}^2(|\mathbf{f}|)$  calculated for the same data used in Figure 7.10 except that the point source is shifted away from the origin. (In the unique case of a point source at the origin, all of the object phases and phase differences are zero, so the phase correlations are all due to noise. Such shifts do not affect  $s_{\Delta\phi}^2(|\mathbf{f}|)$ .) We can clearly extract the same information from this function that we previously extracted from  $s_{\Delta\phi}^2(|\mathbf{f}|)$  in Figure 7.10. For more realistic extended objects  $r_{\Delta\phi}^2(|\mathbf{f}|)$  will retain its general appearance while  $s_{\Delta\phi}^2(|\mathbf{f}|)$  will be smaller, complicating the analysis as discussed above.

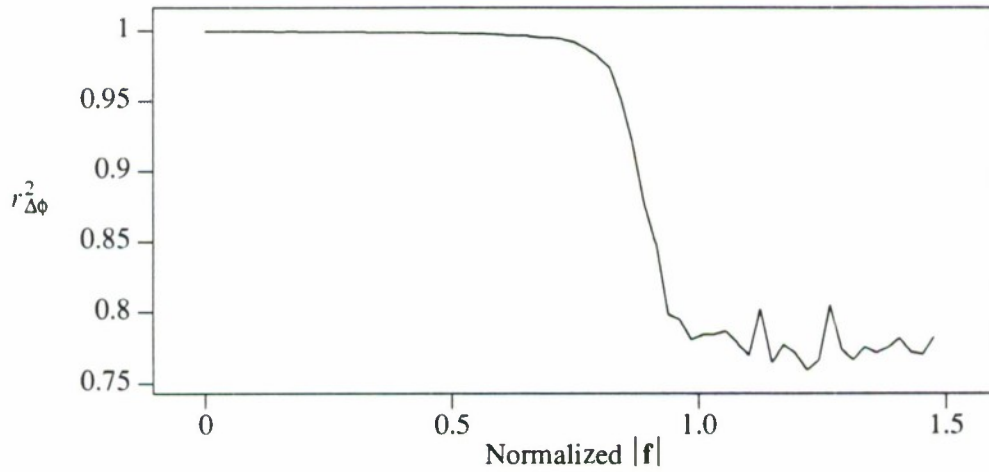


Figure 7.11. Sample correlation function for the data of Fig. 7.10.

The asymptotic correlation value is of course due to discontinuity removal. Using the same type of calculations as before, computing the expected value of  $r_{\Delta\phi}^2(|\mathbf{f}|)$  by integrating the distribution of Figure 7.9(b) produces the value  $3/\sqrt{2}\pi$  or about 0.68 for this limit. Since we use 10 images per set, the actual asymptotic value slightly differs from 0.68.

We are processing these values as if they were part of a single distribution. The theoretical justification for this approach is that although we have different distributions for different spatial frequencies, we do expect roughly constant correlation between spatial frequencies with large magnitudes in a given spatial frequency magnitude range. Those object spatial frequencies which happen to be small will have lower S/N and consequently lower sample correlation. This is why we might want to weight the calculation based on DFT magnitudes or delete the phases associated with small magnitudes from the calculation.



### 7.6.3 Summary

The application of high-resolution optics technologies to space surveillance is more difficult than applying these methods to astronomy. In the face of uncertainty about objects being imaged, their motion, and average atmospheric parameters, data enhancement based on internal evidence becomes more important. To guide this process, data evaluation methods based on the same type of internal measures seem useful.

The evaluation functions defined above represent a useful tool in this process. Certainly more theoretical and experimental work is needed to refine the measures and their interpretation. Additional measures based on the same general philosophy may also be developed in the future. For example, the analytical S/N calculations of Ayers *et al.*<sup>45</sup> could be adapted to this application.

## 8. SUMMARY AND CONCLUSIONS

We have traveled a long road in our effort to understand the new technologies which support high-resolution optical surveillance of space objects. Starting from the basic physics of solar-illuminated imaging theory we have outlined the development of these methods in a quasi-historical fashion. The main goal has been to clearly explain the basic concepts with consistent notation while retaining compatibility with the references.

The reference list is fairly long and reasonably up-to-date although by no means exhaustive. These references along with their references constitute a more complete list of relevant papers. It is certainly essential to consult the literature to obtain a deeper understanding of these topics.

The number of recent papers cited illustrates the great current research interest in speckle imaging. It seems that several very important and interesting papers come out each year. These are primarily from the astronomical community. It is perhaps unfortunate that the adaptive optics literature seems somewhat disjoint from the speckle literature; that is gradually changing as adaptive astronomical projects are proposed and the commonality of the two areas is realized.

It seems wise to pursue experimental work in space surveillance in both adaptive and speckle techniques. The greatest gains will probably come from the combination of these two techniques, but useful experience imaging low-orbit satellites can be obtained using either method.

## APPENDIX A – ANALYTIC SIGNALS

In elementary circuit analysis courses, use is frequently made of the “phasor” for linear systems analysis. A real signal is represented as the real part of a complex signal

$$\cos \omega t = \text{Re}[e^{j\omega t}] \quad (\text{A.1})$$

in order to simplify the calculations. If the single-sided spectrum of the complex phasor passes through a linear system, taking the real part of the result produces the same answer as working with the two-sided spectrum of the sinusoids.

This approach is applicable to constant frequencies only, so it is natural to look for a generalization of the phasor which works on arbitrary waveforms. Such a generalization exists, and is called the analytic signal representation. This representation was originally applied to the study of modulation, but has been found useful in many other areas. Analytic signals are in fact analytic functions as defined in complex analysis, but we need not discuss analyticity in that context. For a more detailed look at analytic signals, consult references such as Dugundji,<sup>69</sup> Bedrosian,<sup>70</sup> Van Trees<sup>71</sup> or Goodman.<sup>4</sup>

Following the idea of the phasor, the analytic representation  $\psi(t)$  of the real signal  $s(t)$  has the following properties:

$$s(t) = \text{Re}[\psi(t)] \quad (\text{A.2})$$

$$\Psi(f) = \begin{cases} 2S(f) & f > 0 \\ 0 & f \leq 0 \end{cases} \quad (\text{A.3})$$

where  $S(f)$  is the Fourier transform of  $s(t)$  and  $\Psi(f)$  is the Fourier transform of  $\psi(t)$ . The factor of two keeps the energy the same.

We can mention some advantages of analytic signals at this point. First, due to the one-sided spectrum, the convolution of one analytic signal with the complex conjugate of another is zero; this greatly simplifies certain manipulations. Second, we can immediately associate the envelope and phase of an analytic signal with its magnitude and phase. These quantities are both fundamental in the study of modulation; in our optical application the magnitude is important.

At this point we know the real part of the analytic representation, which is just the signal itself. We need to determine the imaginary component. In the frequency domain,

$$\Psi(f) = 2S(f)u(f) \quad (\text{A.4})$$

where  $u(f)$  is the unit step function

$$u(f) = \begin{cases} 1 & f \geq 0 \\ 0 & f < 0. \end{cases} \quad (\text{A.5})$$

Expressing this as a convolution in the time domain

$$\psi(t) = 2s(t) * \left[ \frac{\delta(-t)}{2} - \frac{1}{j2\pi t} \right] \quad (\text{A.6})$$

$$= s(t) + j \frac{1}{\pi} \int_{-\infty}^{\infty} \frac{s(\xi)}{\xi - t} d\xi. \quad (\text{A.7})$$



The imaginary part of this expression is known as the Hilbert transform of  $s(t)$ ,  $\hat{s}(t)$ . Hence the analytic signal representation of  $s(t)$  is just  $s(t) + j\hat{s}(t)$ .

We define the complex envelope of the analytic signal  $\psi(t)$  to be  $|\psi(t)|$ , or  $\sqrt{s^2(t) + \hat{s}^2(t)}$ . Similarly, the instantaneous phase of  $\psi(t)$  is defined to be  $\tan^{-1} \frac{\hat{s}(t)}{s(t)}$ .

## APPENDIX B – STRUCTURE FUNCTIONS

Structure functions were originally introduced by Kolmogorov. A couple of useful references are the works by Yaglom<sup>72</sup> and Tatarski,<sup>7</sup> both translated by Richard Silverman. These functions provide a means of bringing the machinery developed for the study of stationary random processes to bear on certain types of non-stationary random processes. We will not be rigorous in distinguishing the various classes of stationarity in this Appendix.

To motivate our discussion, consider the one-dimensional random walk. A particle starts at the origin and then takes a random jump forward or backward one unit each time increment. If  $f(k)$  is the position of the particle at time  $k$ , although  $E[f(k)]$  is zero for all  $k$ , recall that the expected distance of the particle from the origin after  $n$  steps is  $\sqrt{n}$ . In other words, the energy of the process  $f(k)$  increases with  $k$  so the process is not stationary.

If we consider instead the increment process

$$F_T(k) \equiv f(k+T) - f(k) \quad (\text{B.1})$$

we see that this process is stationary. The random jumps expected in any  $T$ -step subintervals are statistically identical.

In this simple example the process  $F$  is exactly stationary. In practical cases, such as meteorological quantities in the atmosphere, the increment process will only be approximately stationary. The approximation is good if no appreciable variation in the process parameters occurs over the increment time  $\tau$ , the continuous analog of the discrete time  $T$  above.

Let  $f(t)$  be a continuous real random process. Without assuming anything about the stationarity of the increment process

$$F_\tau(t) \equiv f(t+\tau) - f(t) \quad (\text{B.2})$$

we want to consider the autocorrelation function of the process  $F$

$$R_F(t_1, t_2) \equiv F_\tau(t_1)F_\tau(t_2). \quad (\text{B.3})$$

An algebraic identity lets us write this using Eq. (B.2)

$$\begin{aligned} R_F(t_1, t_2) = \frac{1}{2} \left\{ \langle [f(t_1 + \tau) - f(t_2)]^2 \rangle + \langle [f(t_1) - f(t_2 + \tau)]^2 \rangle \right. \\ \left. - \langle [f(t_1 + \tau) - f(t_2 + \tau)]^2 \rangle - \langle [f(t_1) - f(t_2)]^2 \rangle \right\} \end{aligned} \quad (\text{B.4})$$

All four terms in this expression are of the form

$$D_f(t_i, t_j) \equiv \langle [f(t_i) - f(t_j)]^2 \rangle \quad (\text{B.5})$$

so if this *structure function* is known, we can calculate the autocorrelation function using Eq. (B.4). This is the reason we work with structure functions.

If the autocorrelation function of a random process is a function only of the difference of the arguments, then the process is stationary. From Eq. (B.4) it follows directly that if the structure function depends only on  $t_i - t_j$ , the increment process is stationary.

It is quite reasonable to work with increments of stationary processes as well. In this case, we find that we can express the structure function in terms of the autocorrelation function

$$D_f(\tau) = 2[R_f(0) - R_f(\tau)]. \quad (\text{B.6})$$

There is much more we could say about structure functions. When investigating unknown random processes, it is sometimes convenient to assume stationarity and look at the power spectrum. If we consider instead the increment process, we buy substantial protection against non-stationarity. Under most conditions, if the process turns out to be stationary we can calculate the autocorrelation function from the structure function.

There is one unnecessary restriction we have imposed here; we have assumed that the process is real. For remarks on the complex case, consult Yaglom.<sup>72</sup>



## REFERENCES

1. J. W. Hardy, "Active Optics: A New Technology for the Control of Light," *Proc. IEEE*, vol. 66, pp. 651-697, June 1978.
2. J. W. Hardy, J. E. Lefebvre, and C. L. Koliopoulos, "Real-Time Atmospheric Compensation," *J. Opt. Soc. Am.*, vol. 67, no. 3, pp. 360-369, March 1977.
3. A. Labeyrie, "Attainment of Diffraction Limited Resolution in Large Telescopes by Fourier Analysing Speckle Patterns in Star Images," *Astron. and Astrophys.*, vol. 6, pp. 85-87, 1970.
4. J. W. Goodman, *Statistical Optics* (Wiley, New York, 1985).
5. A. Papoulis, *Probability, Random Variables, and Stochastic Processes* (McGraw-Hill, New York, 1965).
6. G. L. Rogers, "The Process of Image Formation as the Re-transformation of the Partial Coherence Pattern of the Object," *Proc. Phys. Soc.*, vol. 81, pp. 323-331, 1963.
7. V. I. Tatarski, *Wave Propagation in a Turbulent Medium* (McGraw-Hill, New York, 1961).
8. R. E. Hufnagel and N. R. Stanley, "Modulation Transfer Function Associated with Image Transmission through Turbulent Media," *J. Opt. Soc. Am.*, vol. 54, pp. 52-61, January 1964.
9. D. L. Fried, "Optical Resolution Through a Randomly Inhomogeneous Medium for Very Long and Very Short Exposures," *J. Opt. Soc. Am.*, vol. 56, pp. 1372-1379, October 1966.
10. D. Korff, "Analysis of a Method for Obtaining Near-diffraction-limited Information in the Presence of Atmospheric Turbulence," *J. Opt. Soc. Am.*, vol. 63, pp. 971-980, August 1973.
11. Y. Kim and D. L. Jaggard, "Band-limited Fractal Model of Atmospheric Refractivity Fluctuation," *J. Opt. Soc. Am. A*, vol. 5, no. 4, pp. 475-480, April 1988.
12. J. E. Nelsen, ed., "The Design of the Keck Observatory and Telescope: (Ten Meter Telescope)," Report No. 90, Keck Observatory Science Office, Berkeley, CA, 1985.
13. AVCO, Inc., *AMOS User's Manual, Revision 5* (AVCO Everett Research Laboratory, Everett, Massachusetts, 30 September 1982).
14. J. M. Beckers, F. J. Roddier, P. R. Eisenhardt, L. E. Goad, and K-L. Shu, "National Optical Astronomy Observatories (NOAO) Infrared Adaptive Optics Program I: General Description," *Proc. SPIE*, vol. 628, pp. 290-297, March 1986.
15. R. A. Muller and A. Buffington, "Real-time Correction of Atmospherically Degraded Telescope Images Through Image Sharpening," *J. Opt. Soc. Am.*, vol. 64, no. 9, pp. 1200-1210, September 1974.
16. A. Buffington, F. S. Crawford, R. A. Muller, A. J. Schwemin, and R. G. Smits, "Correction of Atmospheric Distortion with an Image-sharpening Telescope," *J. Opt. Soc. Am.*, vol. 67, no. 3, pp. 298-303, March 1977.
17. A. Buffington, F. S. Crawford, R. A. Muller, and C. D. Orth, "First Observatory Results with an Image-sharpening Telescope," *J. Opt. Soc. Am.*, vol. 67, no. 3, pp. 304-305, March 1977.

18. C. L. Koliopoulos, "Radial Grating Lateral Shear Heterodyne Interferometer," *Appl. Opt.*, vol. 19, no. 9, pp. 1523-1528, May 1980.
19. R. H. Hudgin, "Wave-front Reconstruction for Compensated Imaging," *J. Opt. Soc. Am.*, vol. 67, no. 3, pp. 375-378, March 1977.
20. J. Herrmann, "Least-squares Wave Front Errors of Minimum Norm," *J. Opt. Soc. Am.*, vol. 70, pp. 28-35, 1980.
21. B. R. Hunt, "Matrix Formulation of the Reconstruction of Phase Values from Phase Differences," *J. Opt. Soc. Am.*, vol. 69, pp. 393-399, March 1979.
22. F. Roddier, "Triple Correlation as a Phase Closure Technique," *Optics Comm.*, vol. 60, no. 3, pp. 145-148, November 1986.
23. H. A. McAlister, "Seeing Stars with Speckle Interferometry," *Am. Sci.*, vol. 76, no. 2, pp. 166-173, March-April 1988.
24. A. V. Oppenheim and R. W. Schaffer, *Digital Signal Processing* (Prentice-Hall, Englewood Cliffs, New Jersey, 1975) pp. 541-548.
25. J. W. Goodman and J. F. Belsher, "Fundamental Limitations in Linear Invariant Restoration of Atmospherically Degraded Images," *SPIE*, vol. 75, pp. 141-154, March 1976.
26. L. A. Thompson and C. S. Gardner, "Experiments on Laser Guide Stars at Mauna Kea Observatory for Adaptive Imaging in Astronomy," *Nature*, vol. 328, pp. 229-231, 16 July 1987.
27. K. T. Knox and B. J. Thompson, "Recovery of Images from Atmospherically Degraded Short-exposure Photographs," *Astrophys. J.*, vol. 193, pp. L45-L48, 1974.
28. K. T. Knox, "Image Retrieval from Astronomical Speckle Patterns," *J. Opt. Soc. Am.*, vol. 66, pp. 1236-1239, November 1976.
29. J. C. Fontanella and A. Seve, "Reconstruction of Turbulence-degraded Images Using the Knox-Thompson Algorithm," *J. Opt. Soc. Am. A*, vol. 4, no. 3, pp. 438-448, March 1987.
30. A. W. Lohmann, G. Weigelt, and B. Winitzer, "Speckle Masking in Astronomy: Triple Correlation Theory and Applications," *Appl. Opt.*, vol. 22, no. 24, pp. 4028-4037, 15 December 1983.
31. H. Bartelt, A. W. Lohmann, and B. Winitzer, "Phase and Amplitude Recovery from Bispectra," *Appl. Opt.*, vol. 23, no. 18, pp. 3121-3129, 15 September 1984.
32. G. Weigelt, "Modified Astronomical Speckle Interferometry: Speckle Masking," *Optics Comm.*, vol. 21, pp. 55-59, 1977.
33. J. D. Freeman, J. C. Christou, F. Roddier, D. W. McCarthy, Jr., and M. L. Cobb, "Application of Bispectrum Analysis for Phase Recovery from One-dimensional Infrared Speckle Data," *J. Opt. Soc. Am. A*, vol. 5, no. 3, pp. 406-415, March 1988.
34. R. Barakat and S. Ebstein, "Bispectral Diffraction Imagery. I. The Bispectral Optical Transfer Function," *J. Opt. Soc. Am. A*, vol. 4, no. 9, pp. 1756-1763, September 1987.
35. R. W. Gerchberg and W. O. Saxton, "A Practical Algorithm for the Determination of Phase from Image and Diffraction Plane Pictures," *Optik*, vol. 35, pp. 237-246, 1972.

36. J. R. Fienup, "Reconstruction of an Object from the Modulus of its Fourier Transform," *Opt. Lett.*, vol. 3, no. 1, pp. 27-29, 1978.
37. J. R. Fienup, "Space Object Imaging Through the Turbulent Atmosphere," *Opt. Engr.*, vol. 18, no. 5, pp. 529-534, September-October 1979.
38. J. C. Dainty and J. R. Fienup, "Phase Retrieval and Image Reconstruction for Astronomy," in *Image Recovery: Theory and Application*, ed. H. Stark (Academic Press, New York, 1987).
39. M. H. Hayes, "The Unique Reconstruction of Multidimensional Sequences from Fourier Transform Magnitude or Phase," in *Image Recovery: Theory and Application*, ed. H. Stark (Academic Press, New York, 1987).
40. A. Levi and H. Stark, "Restoration from Phase and Magnitude by Generalized Projections," in *Image Recovery: Theory and Application*, ed. H. Stark (Academic Press, New York, 1987).
41. J. A. Cadzow, "Signal Enhancement – A Composite Property Mapping Algorithm," *IEEE Trans. Acoust. Speech Signal Processing*, vol. 36, pp. 49-62, January 1988.
42. J. C. Dainty, "Stellar Speckle Interferometry," in *Laser Speckle and Related Phenomena*, ed. J. C. Dainty (Springer-Verlag, New York, 1975).
43. J. C. Dainty and A. H. Greenaway, "Estimation of Spatial Power Spectra in Speckle Interferometry," *J. Opt. Soc. Am.*, vol. 69, no. 5, pp. 786-790, May 1979.
44. P. Nisenson and C. Papaliolios, "Effects of Photon Noise on Speckle Image Reconstruction with the Knox-Thompson Algorithm," *Optics Comm.*, vol. 47, no. 2, pp. 91-96, August 1983.
45. G. R. Ayers, M. J. Northcott, and J. C. Dainty, "Knox-Thompson and Triple-correlation Imaging through Atmospheric Turbulence," *J. Opt. Soc. Am. A*, vol. 5, no. 7, pp. 963-985, July 1988.
46. M. G. Miller, "Noise Considerations in Stellar Speckle Interferometry," *J. Opt. Soc. Am.*, vol. 67, no. 9, pp. 1176-1184, September 1977.
47. C. Roddier and F. Roddier, "Influence of Exposure Time on Spectral Properties of Turbulence-degraded Astronomical Images," *J. Opt. Soc. Am.*, vol. 65, no. 6, pp. 664-667, June 1975.
48. D. P. Karo and A. M. Schneiderman, "Speckle Interferometry at Finite Spectral Bandwidths and Exposure Times," *J. Opt. Soc. Am.*, vol. 68, no. 4, pp. 480-485, April 1978.
49. K. A. O'Donnell and J. C. Dainty, "Space-Time Analysis of Photon-Limited Stellar Speckle Interferometry," *J. Opt. Soc. Am.*, vol. 70, no. 11, pp. 1354-1361, November 1980.
50. F. Roddier, "Interferometric Imaging in Optical Astronomy," *Phys. Rep.*, (to be published).
51. J. Ohtsubo, "Effects of Finite Spectral Bandwidth and Focusing Error on the Transfer Function in Stellar Speckle Interferometry," *J. Opt. Soc. Am. A*, vol. 2, no. 5, pp. 667-673, May 1985.
52. J. Ohtsubo, T. Eiju, K. Tomita, M. Noguchi, T. Kanda, and T. Kohno, "Effect of Spectral Bandwidth on the MTF in Stellar Speckle Interferometry," *Optics Comm.*, vol. 65, no. 2, pp. 79-83, 15 January 1988.
53. A. M. Schneiderman and D. P. Karo, "How to Build a Speckle Interferometer," *Opt. Engr.*, vol. 16, no. 1, pp. 72-79, January-February 1977.



54. D. L. Fried, "Varieties of Isoplanatism," *SPIE*, vol. 75, pp. 20-29, March 1976.
55. D. Korff, G. Dryden, and R. Leavitt, "Isoplanicity: The Translation Invariance of the Atmospheric Green's Function," *J. Opt. Soc. Am.*, vol. 65, no. 11, pp. 1321-1330, November 1975.
56. A. M. Schneidman and D. P. Karo, "Speckle Interferometry Measurements of Atmospheric Non-isoplanicity Using Double Stars," *J. Opt. Soc. Am.*, vol. 68, no. 3, pp. 338-347, March 1978.
57. P. Nisenson and R. V. Stachnik, "Measurements of Atmospheric Isoplanatism Using Speckle Interferometry," *J. Opt. Soc. Am.*, vol. 68, no. 2, pp. 169-175, February 1978.
58. J. Ebersberger and G. Weigelt, "Isoplanicity and Lifetime of Stellar Speckle Interferograms," *Optica Acta*, vol. 32, no. 7, pp. 793-801, 1985.
59. J. C. Christou and E. K. Hege, "Isoplanicity Measurements for Calibration of Speckle Holography Amplitudes," *Optics Comm.*, vol. 58, no. 1, pp. 4-10, May 1986.
60. C. Y. C. Liu and A. W. Lohmann, "High Resolution Image Formation Through the Turbulent Atmosphere," *Optics Comm.*, vol. 8, no. 4, pp. 372-377, August 1973.
61. R. H. T. Bates, P. T. Gough, and P. J. Napier, "Speckle Interferometry Gives Holograms of Multiple Star Systems," *Astron. and Astrophys.*, vol. 22, pp. 319-320, 1973.
62. C. Papaliolios, P. Nisenson, and S. Ebstein, "Speckle Imaging with the PAPA Detector," *Appl. Opt.*, vol. 24, no. 2, pp. 287-292, January 1985.
63. T. Gonsiorowski, "A New Product for Photon-Limited Imaging," *Proc. SPIE*, vol. 627, pp. 626-630, 1986.
64. F. J. Roddier and C. Roddier, "National Optical Astronomy Observatories (NOAO) Infrared Adaptive Optics Program II: Modeling Atmospheric Effects in Adaptive Optics Systems for Astronomical Telescopes," *Proc. SPIE*, vol. 628, pp. 298-304, March 1986.
65. B. P. Lathi, *Signals, Systems and Communication* (Wiley, New York, 1965).
66. T. S. Huang, J. W. Burnett, and A. G. Deczky, "The Importance of Phase in Image Processing Filters," *IEEE Trans. Acoust. Speech Signal Processing*, vol. 23, no. 6, pp. 529-542, December 1975.
67. A. V. Oppenheim and J. S. Lim, "The Importance of Phase in Signals," *Proc. IEEE*, vol. 69, no. 5, pp. 529-541, May 1981.
68. N. J. Bershad and A. J. Rockmore, "On Estimating Signal-to-Noise Ratio Using the Sample Correlation Coefficient," *IEEE Trans. Inf. Thy.*, vol. 20, pp. 112-113, January 1974.
69. J. Dugundji, "Envelopes and Pre-Envelopes of Real Waveforms," *IRE Trans. Inf. Thy.*, pp. 53-57, March 1958.
70. E. Bedrosian, "The Analytic Signal Representation of Modulated Waveforms," *Proc. IRE*, vol. 50, pp. 2071-2076, October 1962.
71. H. L. Van Trees, *Detection, Estimation, and Modulation, Part III* (Wiley, New York, 1971).
72. A. M. Yaglom, *An Introduction to the Theory of Stationary Random Functions* (Dover Publications, New York, 1973).

## REPORT DOCUMENTATION PAGE

1a. REPORT SECURITY CLASSIFICATION Unclassified			1b. RESTRICTIVE MARKINGS		
2a. SECURITY CLASSIFICATION AUTHORITY			3. DISTRIBUTION/AVAILABILITY OF REPORT Approved for public release; distribution unlimited.		
2b. DECLASSIFICATION/DOWNGRADING SCHEDULE					
4. PERFORMING ORGANIZATION REPORT NUMBER(S) Technical Report 819			5. MONITORING ORGANIZATION REPORT NUMBER(S) ESD-TR-88-221		
6a. NAME OF PERFORMING ORGANIZATION Lincoln Laboratory, MIT		6b. OFFICE SYMBOL (If applicable)	7a. NAME OF MONITORING ORGANIZATION Electronic Systems Division		
6c. ADDRESS (City, State, and Zip Code) P.O. Box 73 Lexington, MA 02173-0073			7b. ADDRESS (City, State, and Zip Code) Hanscom AFB, MA 01731		
8a. NAME OF FUNDING/SPONSORING ORGANIZATION Air Force Systems Command, USAF		8b. OFFICE SYMBOL (If applicable)	9. PROCUREMENT INSTRUMENT IDENTIFICATION NUMBER F19628-85-C-0002		
8c. ADDRESS (City, State, and Zip Code) Andrews Air Force Base Washington DC 20334			10. SOURCE OF FUNDING NUMBERS		
			PROGRAM ELEMENT NO. 12424F, 31310F, 63223C	PROJECT NO. 80	TASK NO. WORK UNIT ACCESSION NO.
11. TITLE (Include Security Classification) New Techniques for High-Resolution Optical Space Surveillance					
12. PERSONAL AUTHOR(S) Timothy P. Wallace					
13a. TYPE OF REPORT Technical Report		13b. TIME COVERED FROM _____ TO _____		14. DATE OF REPORT (Year, Month, Day) 1988, November, 2	
15. PAGE COUNT 88					
16. SUPPLEMENTARY NOTATION None					
17. COSATI CODES			18. SUBJECT TERMS (Continue on reverse if necessary and identify by block number)		
FIELD	GROUP	SUB-GROUP	optical space surveillance		
			statistical optics		
			atmospheric turbulence		
			adaptive optics		
			speckle imaging		
			phase retrieval		
			light propagation		
			optical data evaluation		
19. ABSTRACT (Continue on reverse if necessary and identify by block number)					
<p>The problem of imaging through atmospheric turbulence has plagued astronomers for centuries. Only in the last 20 years has the lost resolution been restored through innovative hardware and algorithms. This report discusses the new optical imaging technologies of adaptive optics and speckle imaging in the space surveillance context. The techniques are compared and contrasted, and new imaging methods are proposed which combine elements of both. New methods are suggested for optical data evaluation.</p>					
20. DISTRIBUTION/AVAILABILITY OF ABSTRACT <input type="checkbox"/> UNCLASSIFIED/UNLIMITED <input checked="" type="checkbox"/> SAME AS RPT. <input type="checkbox"/> DTIC USERS			21. ABSTRACT SECURITY CLASSIFICATION Unclassified		
22a. NAME OF RESPONSIBLE INDIVIDUAL Lt. Col. Hugh L. Southall, USAF			22b. TELEPHONE (Include Area Code) (617) 981-2330		22c. OFFICE SYMBOL ESD/TML